OAK RIDGE NATIONAL LABORATORY
operated by
UNION CARBIDE CORPORATION
NUCLEAR DIVISION
for the
U.S. ATOMIC ENERGY COMMISSION

UNION CARBIDE

ORNL - TM - 1753

58

INELASTIC SCATTERING OF 40-MeV POLARIZED PROTONS

(Thesis)

Martin P. Fricke

Submitted to the Faculty of the Graduate School of the University of Minnesota in partial fulfillment of the requirements for the Degree of Doctor of Philosophy.

DISCLAIMER

ORNL-TM-1753

Inelastic Scattering of 40-MeV Polarized Protons

A THESIS
SUBMITTED TO THE FACULTY OF THE GRADUATE SCHOOL
OF THE UNIVERSITY OF MINNESOTA

By

Martin P. Fricke

IN PARTIAL FULFILLMENT OF THE REQUIREMENTS
FOR THE DEGREE OF
DOCTOR OF PHILOSOPHY

MARCH 1967

OAK RIDGE NATIONAL LABORATORY
Oak Ridge, Tennessee
Operated by
UNION CARBIDE CORPORATION
for the
U. S. ATOMIC ENERGY COMMISSION

ABSTRACT

The left-right asymmetry and differential cross section for the inelastic scattering of 40-MeV polarized protons were measured over a large angular region for each of the following 2^+ excitations: 1.78 MeV in ^{28}Si, 1.41 and 2.97 MeV in ^{54}Fe, 1.45 MeV in ^{58}Ni, and 1.33 MeV in ^{60}Ni. Some asymmetry and cross-section data were also obtained for 3^- states: 6.9 MeV in ^{28}Si, 4.8 and 6.4 MeV in ^{54}Fe, 4.5 MeV in ^{58}Ni, and 4.08 MeV in ^{60}Ni. Elastic polarization and cross-section data were obtained for each target. The inelastic scattering was analyzed in distorted-wave approximation using the collective-model extension of the optical-model potential determined by fitting the elastic scattering. The inelastic asymmetry and cross-section data are best reproduced with a collective-model interaction obtained by deforming the complete optical potential, including its imaginary and spin-orbit parts.

TABLE OF CONTENTS

I. INTRODUCTION

This thesis is primarily concerned with the measurement and analysis of the left-right asymmetry produced in the inelastic scattering of medium-energy polarized protons, a property for which very few results have been previously obtained. More specifically, we have measured the asymmetry of 40-MeV protons for 2^+ and 3^- excitations in some even-even nuclei. To estimate the significance of these data in terms of the current theoretical structure, we first review the situation for inelastic cross sections.

In recent years, a large number of cross sections for the inelastic scattering of 8- to 55-MeV protons have been analyzed[1,2,3] assuming a collective-model generalization of the optical model.[4,5,6] In this treatment, the optical-model potential found to reproduce the observed elastic scattering is made non-spherical, and the non-spherical part induces transitions to vibrational or rotational states of the target nucleus. The free parameters in the model are the multipole order ℓ of the transition and its strength, or deformation parameter, β_ℓ; these are deduced by comparison to the shape and magnitude, respectively, of the measured differential cross section.

Distortion of the scattering wave functions, the "elastic" distortion described by the optical potential, has a strong influence on direct reactions; and computer codes[7] are necessary

to permit a careful treatment of this complication. Since the introduction of these codes, the collective-model analysis has proved phenomenally successful in accounting for proton inelastic scattering data. Most of these data are for low-lying quadrupole (2^+) and octupole (3^-) transitions in even-mass nuclei, and have been successfully reproduced by assuming a simple, single-step excitation appropriate for a 2^ℓ-pole rotation or single-phonon surface oscillation.[6] Unless the coupling between the ground and excited states is uncommonly strong,[8] such transitions induced by medium-energy protons can be treated in the distorted-waves (DW) approximation,[5,6] as is discussed further in Section III. For 40-MeV protons, the collective-model, DW treatment has given good predictions of the detailed shape of the angular distribution for states ranging from the 1.37-MeV 2^+ in ^{24}Mg,[2] with $\beta_2 = 0.47$, to the 3.2-MeV 5^- in ^{208}Pb,[3] with $\beta_5 = 0.06$. Inelastic scattering data from odd-mass nuclei have also been interpreted with the collective model, assuming the odd particle or hole is coupled to a collective excitation of the core.[9] Some proton data for more complicated collective transitions involving multiple excitation through one or more excited states have been successfully described using, instead of the DW method, the related coupled-equations[10] technique (see Section III). Except perhaps for the weaker excitations, where the collective character of the states is not well founded, the deformation

parameters deduced from such analyses of inelastic proton scattering seem to agree well with those similarly obtained for other projectiles, for different energies, and with Coulomb excitation results. The agreement is generally within 20 to 30 percent.* These β_ℓ's therefore appear to constitute a basic measure of the interaction strength, a useful place to test more advanced theories capable of predicting these strengths from a more detailed, or "microscopic", description[11] of the interaction and nuclear wave functions.

One such microscopic description of inelastic scattering at high energies has been formulated by use of the impulse approximation,[12] and has been successfully applied[13] to both cross sections and polarizations for 156-MeV protons. Since this approach assumes free two-nucleon scattering amplitudes, it may not be valid for protons of energy less than about 100 MeV. (No phenomenological test of the matter by comparison to lower-energy data has yet been published.) An alternative microscopic approach for lower energy scattering is currently being investigated by Satchler[14] and others[15,16] in which the interaction is taken to be a sum of projectile-

*The agreement for different projectiles is sometimes, but not always, better for the "deformation length" $\beta_\ell R_0$ (where R_0 is the nuclear-radius parameter) than for the deformation parameter β_ℓ. Which of these should be the more fundamental parameter is not fully resolved to date; β_ℓ is used here.

nucleon (two-body) forces of phenomenological form. The inelastic scattering transition amplitude is then evaluated for this interaction in DW approximation using shell-model wave functions for the nuclear ground and excited states,* with no free parameter determining the relative strengths of different transitions. In principle, this approach is also capable of describing 0^+, 1^-, and unnatural parity $\left[\pi = (-)^{J+1}\right]$ excitations in even nuclei, for which no straightforward predictions are possible in the framework of first-order (DW), collective-model calculations. This type of microscopic analysis has been applied to the cross sections for the inelastic scattering of 18.8-MeV protons from ^{90}Zr,[17] 11- and 40-MeV protons from nickel isotopes,[15] and of 17.5-MeV protons from four N = 28 nuclei.[16] In general, these calculations for the first 2^+ states have involved real-valued form factors (as defined in Section III) with radial shapes which agree only crudely with the collective-model result obtained by deforming the real, central part of the optical potential. The shapes of the calculated differential cross sections were, however, very similar to the collective-model

---

*To test the validity of the interaction assumed, it may prove desirable to examine first the weaker, non-collective transitions which involve simpler nuclear wave functions. The inelastic scattering cross sections for 18.8-MeV protons on ^{90}Zr have been successfully described[17] with this treatment for a number of levels attributed to $g_{9/2}{}^2$ and $g_{9/2}p_{1/2}$ proton configurations by assuming a Yukawa interaction, of range 1.0 F and strength 205 MeV, between the incident and target protons.

predictions. This contributes to the prevalent impression that the shape of the cross section is largely determined by the angular momentum transfer and the elastic distortion, and is somewhat insensitive to the detailed form of the coupling interaction.

At present it appears that measurements of the polarization produced in inelastic proton scattering, or of the left-right asymmetry produced in the inelastic scattering of a polarized beam, can contribute to our understanding of this reaction in several ways. Perhaps the most specific question which can be answered by the present data for 2^+ and 3^- excitations is whether or not they are reproduced by the collective-model calculation found so successful for the cross sections. In particular the cross sections have seemed well described by a deformation of the central part of the optical potential and have presented no obvious demand for a spin-dependent term in the coupling interaction, and no such term has previously been included. It is of interest to see if the asymmetries require a spin dependence of the form implied in the collective-model approach, that obtained by deforming also the non-central, $\vec{\sigma} \cdot \vec{\ell}$ part of the optical potential.* Together with measurements of p'-γ angular

---

*The inelastic asymmetry does not vanish in the absence of a spin-dependent coupling interaction, due to the $\vec{\sigma} \cdot \vec{\ell}$ term in the optical potential for the distorted waves.

correlations, inelastic polarization and asymmetry data could also yield information on the importance of spin flip in natural-parity excitations.[14]

But the relevance of the present asymmetry measurements is not limited to questions of the proper spin dependence for the inelastic interaction. Past[18] and present calculations indicate that the asymmetry is quite sensitive to other aspects of the collective-DW calculation. For example, these data will be shown to present a strong demand for complex coupling, in which both real and imaginary parts of the central optical potential contribute to the non-spherical interaction.[19] The effect of this imaginary interaction on the asymmetry seems sufficiently dramatic to forecast little chance of success for a microscopic form factor applied to these data which does not have some similar imaginary component. The inelastic asymmetry calculations are also quite sensitive to the optical-model parameters, through both the elastic distortion and the collective-model form factors. This was to some extent anticipated, and the choice of 40-MeV bombarding energy was influenced by a desire to take advantage of previous optical-model studies[20,2] of elastic scattering at this energy. Analysis of the present inelastic asymmetry data has in fact required a further study of the elastic data, and the optical-model parameters found are somewhat different from the latest 40-MeV results.[21] The new parameters simultaneously improve the agreement with both the elastic polarization and the inelastic asymmetry.

When this experiment was begun, in the fall of 1964, there were no published measurements of inelastic asymmetry or polarization for protons of energy between 15 and 150 MeV on any target other than ^{12}C.[22] In the past year, inelastic asymmetry data have been presented for the 4.43-MeV (2^+) state in ^{12}C for protons of energy 16.5 MeV,[23] 20 to 28 MeV,[24] and 30,[25] 40,[20], and 50 MeV,[25] and for the 1.78-MeV (2^+) state in ^{28}Si at 30 and 50 MeV.[25] Data for 2^+ states in heavier targets have been recently obtained at Saclay for 16.5- and 18.6-MeV protons. The 1.33-MeV excitation in ^{60}Ni and the 1.17-MeV excitation in ^{62}Ni were measured[23] at 16.5 MeV; and the following quadrupole transitions were observed[26] at 18.6 MeV: 0.99 MeV in ^{48}Ti, 1.57 MeV in ^{50}Ti, 1.43 MeV in ^{52}Cr, 1.41 and 2.97 MeV in ^{54}Fe, and 0.84 MeV in ^{56}Fe. Collective-model calculations have been made for the carbon and silicon data at 30 and 50 MeV,[25] and for the nickel data at 16.5 MeV,[27] with generally negative results (as is discussed in Section III).

The present work presents 40-MeV proton asymmetry data taken at the Oak Ridge Isochronous Cyclotron (ORIC) for the 2^+ states at 1.78 MeV in ^{28}Si, 1.41 and 2.97 MeV in ^{54}Fe, 1.45 MeV in ^{58}Ni, and 1.33 MeV in ^{60}Ni. Some asymmetry data were also obtained for 3^- excitations at 6.9 MeV in ^{28}Si, 6.4 MeV in ^{54}Fe, 4.5 MeV in ^{58}Ni, and 4.08 MeV in ^{60}Ni. The inelastic cross section was obtained

for each of these states and for the 4.8-MeV (3^-) level in ^{54}Fe; the elastic cross sections and polarizations were also obtained for each target. Preliminary results of the present measurements and their analysis have been reported elsewhere[28,21] at various stages of the project.

In Section II the experiment is described, and the data are discussed. An optical-model analysis of the elastic scattering, and a collective-DW analysis of the inelastic scattering, are presented and discussed in Section III. Comments on the main results and suggestions for further work are given in Section IV. Acknowledgements appear in Section V and references in Section VI. In Section VII, the data are listed in tabular form; all other tables and graphical presentations are included in the text.

II. EXPERIMENT

The main experimental difficulty in the measurement of inelastic asymmetry was to achieve a satisfactory compromise between intensity and energy resolution. Even for the strongly excited, well-separated collective levels studied here, this placed stringent requirements on the beam of polarized protons. There was no internal source of polarized protons for the ORIC cyclotron, and the beam was polarized externally by elastic scattering from calcium, prior to the target where the asymmetry measurements were made. For the final, optimized system a 40-MeV proton beam was obtained at the target which had a polarization of 27.4 percent and an energy spread of 500 keV. The price paid for this is seen in the intensity achieved at the target of 10^8 protons/sec, a factor of over 10^6 less than that where the beam emerged from the cyclotron.

In addition to the problem of beam preparation, asymmetry measurements place strong emphasis on an efficient accumulation of data. In order to measure the asymmetry in the elastic scattering of 40-MeV protons,[20] an array of 32 NaI(Tl) counters had been developed previously[29] at the ORIC laboratory for use in conjunction with a 20,000-channel pulse-height analyzer. This equipment was also used in the present work. The counter resolution, about 500 keV, was adequate to measure the inelastic scattering for several

excitations; and this amount was matched by the energy spread in the polarized proton beam developed for the present experiment. However, the counter resolution was in fact the major limitation in the inelastic measurements. If these data are to be improved, or extended for transitions which are less enhanced, use of detectors with better resolution should be a prime consideration.

In this Section, the preparation of the beam and measurement of its polarization are described. The counting system and its performance for the present measurements are discussed. Other experimental details of the running procedure, alignment checks, target material, data reduction, and error analysis are also given here. Finally, the data are presented and compared to other measurements made with medium-energy protons.

1. Polarized-Proton Beam

Proton polarization experiments[20] at 40-MeV energy were well underway at the ORIC laboratory at the time when the present experiment was designed. With an amendment to the existing beam-preparation equipment, these measurements were then extended to inelastic scattering. In Fig. 1 the beam optics system is shown in its latest form. The new elements are the analyzing magnet and quadrupole triplet (Q12) shown

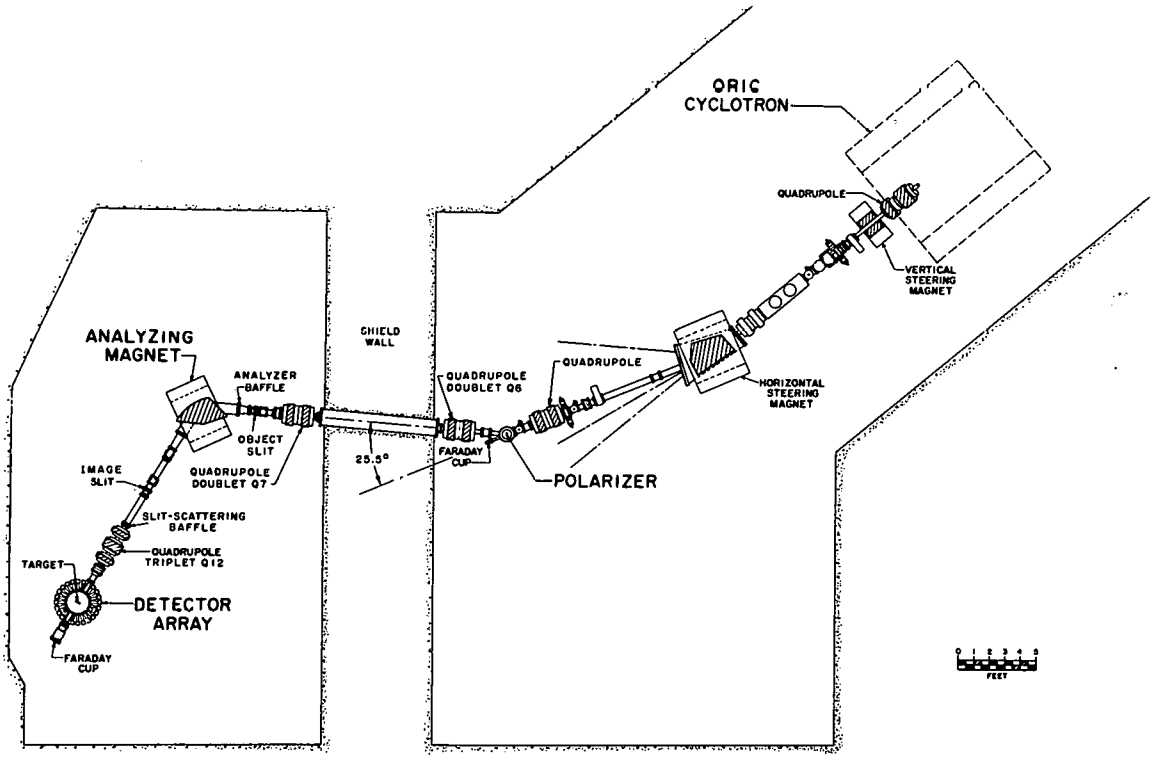

Figure 1. Beam preparation system for polarized protons. Other sections of the ORIC beam-handling system, used for other experiments, are not shown here.

in front of the second scattering chamber. (This chamber was previously located behind the quadrupole doublet Q7, which was slightly farther away from the shield wall.)

The beam-preparation system has evolved continuously into its present form. This evolution was possible because the ORIC cyclotron[30] is an azimuthally-varying-field machine capable of accelerating different particles to different energies. The polarized beam was originally[20,29] made from proton recoils produced by 80-MeV alpha particles bombarding a hydrogen gas target. Previous measurements[31] of p + ^{4}He polarization had indicated that a large polarization would be achieved for the protons at 25.5° (in the laboratory system of reference). A scattering chamber for the gas target and beam-handling equipment consisting principally of magnets to position and focus the alpha and proton beams were constructed and located accordingly.[29] The resultant 40-MeV proton beam at the second target had a polarization of 82 percent, intensity 2×10^7 protons/sec, and an energy spread of 1.4 MeV arising mainly from kinematic spread in the α-p scattering. Together with a typical resolution of 500 keV for the NaI counters used to measure the elastic scattering from the second target, the experiments were limited to only a few nuclei with large separations between the ground and first excited states: ^{12}C, ^{40}Ca, ^{90}Zr, and ^{208}Pb. But these measurements revealed that ^{40}Ca had a

relatively large polarization and cross section for 40-MeV protons at 25.5°. It could therefore be used as a replacement for the α-p polarizer to reduce the kinematic energy spread, without requiring a major overhaul of the beam-preparation system to accommodate a different scattering angle. An 800-keV-thick (0.05 cm) polarizer target of natural calcium (96.97 percent ^{40}Ca) was then used to produce by elastic scattering a beam of 40-MeV protons which, at the second target, had a polarization of 35 percent, intensity 8×10^7 protons/sec, and an energy spread of 600 keV. This was adequate to expand the elastic polarization survey but not quite adequate for inelastic scattering, due to the presence of inelastic proton groups and general background from the Ca polarizer. Most significantly for later work, the elastic program was extended to a study of the energy variation of Ca scattering by performing a series of double-scattering experiments at 35, 40, and 45 MeV.[32]

The results of the elastic scattering measurements for calcium indicated that an adequate polarization and cross section would be obtained at 25.5° for proton energies at least as high as 45 MeV. To study the inelastic scattering of 40-MeV polarized protons, we then decided to use 50-MeV protons on a 10-MeV-thick (0.607 cm) natural Ca polarizer, with magnetic energy analysis of the scattered beam. Estimates of the energy spread vs intensity, and of the heat-transfer

problem of dissipating energy lost in the Ca target, were also encouraging for a 10-MeV-thick polarizer. Subsequent measurements have shown that, with the plane of the polarizer target oriented to bisect the angle between the incident and scattered beam (a "tilt" of 12.75°), the energy spread in the 40-MeV beam thus produced is less than 1 MeV. The calcium target was installed in its evacuated scattering chamber by bolting it to a water-cooled aluminum frame. Under these conditions it has survived an average beam current of 15 μA for about 300 hours without noticeable deterioration.

A. Beam Transport and Energy Analysis

As shown in Fig. 1, a "primary" optics system[33,34] transports the 50-MeV (unpolarized) proton beam from the exit of the ORIC cyclotron and focuses it to a spot, about 10 mm wide by 2 mm high, on the calcium polarizer.* Very little (about ten percent) loss of beam is suffered up to this point, and 18 μA of protons were commonly achieved at the polarizer. The vertical and horizontal position of the beam there is

---

*This is the same system as was used for work done with the α-p and thin Ca polarizers. For that work, a focusing arrangement involving this horizontally elongated spot at the polarizer was found[29] to best match the operation of quadrupole lenses Q6 and Q7 to produce an optimum focus, with a vertically elongated spot, at the target. (The target was located at the focus of Q7.) The requirements for the present system are almost identical, and the primary-optics focusing arrangement could be carried over entirely.

adjustable with the vertical and horizontal steering (sector) magnets. The beam spot at the polarizer is the source for a "secondary" optics system, which collects the 40-MeV (polarized) beam emerging near 25.5°, energy-analyzes it, and focuses it onto the second target. For the present work, beam-optics calculations were made to optimize the design of this secondary optics system, with a mind toward using the existing 25.5° hole in the shield wall, lenses Q6 and Q7, and some extra quadrupole elements and a bending magnet which were available at the time.

A number of possible configurations was considered for the secondary system in which the beam would start out along the 25.5° scattering line, end up inside the experiment room, and pass through reasonable magnetic fields in between. There are in fact not many of these, and the general arrangement shown in Fig. 1 suggested itself: Q7 would focus the beam onto an object slit for a sector magnet, and a quadrupole lens would transport the beam from the image slit to the target. In this way, the image slit would not be directly in front of the scattering chamber, as a possible source of background; and some baffling for slit-scattered protons could also be considered. The questions of the sector-magnet parameters suitable for the desired resolution and prevailing space limitations were considered next. Using first-order optics theory,[35] a range of solutions for the

magnet design (radius, angle of bend, field homogeneity, and entrance-and-exit angles) was found which would achieve a resolution of 500 keV and involve object and image lengths compatible with the operation of, say, a symmetric[36] quadrupole triplet in the image space. At this point, then, attention was paid to the available equipment and to the crucial problem of efficient beam transmission.

The bending magnet used was available from the "86-inch" 22-MeV proton cyclotron facility at Oak Ridge. This is a homogeneous-field inflection spectrometer, which was previously operated[37] with a bending angle $\Phi = 75°$ (in the opposite sense as is now used), a mean radius $r_0 = 24$ inches, and entrance and exit angles[35] $\epsilon_1 = 55°$ and $\epsilon_2 = -19.5°$, respectively. Its excitation curve (field vs current) was measured and found to saturate strongly near 15 kilogauss. This magnet could therefore be used (upside down) in the present application by fabricating a new vacuum envelope to accommodate a mean radius of 27.46 inches, which reduces the required field to 13.23 kilogauss for 40-MeV protons. The new envelope also permitted an increase in the gap width from 1-1/8 inches to 1-5/8 inches, by adding spacers to the magnet yoke and by making the magnet pole tips an integral part of the vacuum envelope, as opposed to using a separate tank.

Use of a different mean radius for the same pole pieces also changes Φ, ε_1, and ε_2 from their original values, and fixing these four parameters permits only one arrangement (object and image lengths and resultant magnification) if double focusing is desired. This, however, was not very important since a radial, or horizontal, single-focusing solution could be attained for the analyzer; and a net double-focusing at the image slit could be achieved through the action of both the analyzer and the doublet lens Q7, located immediately upstream. For a minimum modification of the beam trajectory across the pole face of the magnet (with the entrance and exit points remaining unchanged), the new center of curvature for the central ray was taken along the bisector of the original sector angle. The resulting magnet parameters are $r_0 = 27.46$ inches, $\Phi = 64.3°$, $\varepsilon_1 = 49.65°$, and $\varepsilon_2 = -24.85°$. For these, a double-focusing situation is obtained for an object length $\ell_0 = 0.61\ r_0$ (and image length $2.81\ r_0$), and promising single-focusing conditions range from this to $\ell_0 = 1.6\ r_0$ (where the image distance for radial focusing is $\ell_r = 1.92\ r_0$). For shorter object distances the radial magnification becomes forebodingly large, and for longer object distances the axial (vertical) defocusing becomes prohibitive. This range of object lengths also closely matches that allowed by space considerations.

The quadrupole Q12 was made up from three elements available at ORIC with an aperture-diameter of three inches. Two of these are 4 inches long and the third (middle) element is 8 inches long. Their excitation curves were measured, and the field gradients were found to be very constant for excitations up to five kilogauss/inch. This field and the space limitations allowed a number of different doublet and triplet arrangements to be considered for transporting the beam from the image slit to the chamber. For both the quadrupole and analyzer magnets, no solution was apparent which would have been superior to that found possible with the existing equipment, and its use saved a considerable amount of time.

Using the magnet parameters established from these general considerations, a series of detailed computer calculations was made to optimize the transmission of the secondary optics system. This was done using the code "OPTIK",[38] a first order beam-optics program especially appropriate for a long train of magnet elements where matrix methods are desirable. The program represents each magnet element as a linear operator in the six-dimensional vector space of the beam particle's transverse position and momentum, central magnetic rigidity, and fractional deviation from the central rigidity. Quadrupole field gradients can be searched upon to yield specified beam conditions, and the components

of selected source vectors can be traced through the system. Of most significance here, an aperture stop (beam pipe opening, magnet gap, etc.) specified at some point in the system is transferred back to the source through the inverse product matrix evaluated up to that point. In this way, the phase-space volume of beam accepted by that stop, and of all other stops in the system, can be mapped out at the source of particles. For these detailed calculations, the quadrupole lengths and the analyzer pole boundaries were corrected for fringing field according to previous experience at the ORIC laboratory,[33,34] by adding one inch to the physical length of each quadrupole element and by extending both analyzer field boundaries by an amount 0.64 times the gap width (1-5/8 inches).

OPTIK calculations were made for the secondary system, from the calcium polarizer to the target, for analyzer object lengths varying in eight steps between $\ell_0 = 0.61\ r_0$ and $\ell_0 = 1.6\ r_0$ (with ℓ_r determined by the requirement of single focusing). This was done for different positions of the quadrupole doublet Q7, and for various arrangements of a quadrupole lens in the image space (its distance from the image slit and target, the number of elements used, their separation, and their order of focusing or defocusing). For each of these cases, the following focusing conditions were investigated for the combined action of lens Q7 and the

analyzing magnet: (i) axial focusing at 0.3 r_0, 0.5 r_0, 0.6 r_0, and 0.7 r_0 before the entrance boundary of the analyzer (between the object slit and the magnet); (ii) axial focusing at the image slit (double focusing); (iii) beam made axially parallel at the image slit; and (iv) beam made axially parallel at the object slit. (In each instance, Q7 produces a radial focus at the object slit, and the analyzer focuses radially at the image slit.) For all of these possibilities, the phase-space acceptance determined by the physical apertures of the system was evaluated and compared to the known phase volume occupied by the source of particles from the calcium target (known spot size and desirable angular divergence). A baffle at the entrance to the analyzer, to shield the beam pipe past the image slit from any possible proton trajectory, and one before Q12 to intercept slit-scattering, could also be designed from these phase-space projections.

The optimum focusing arrangement proved to be the case of double focusing at the image slit using $\ell_0 = 1.0\ r_0$, with a quadrupole triplet (Q12) operated symmetrically in the image space. For this, the maximum energy spread in the analyzed beam, assuming no aberrations, would be 500 keV for object and image slits each of total width 0.423 cm. The phase-space acceptance of the entire secondary optics system evaluated at the polarizer for a monoenergetic beam corresponds to a value (transverse displacement from the

optic axis times transverse angular divergence) of 1.5×10^{-2} cm-radian for the radial (horizontal) coordinates, and 3.3×10^{-2} cm-radian for the axial (vertical) coordinates. These "areas" are approximately rectangular: for a radial distance of up to ± 0.53 cm from the center of the polarizer, a radial angular divergence of up to ± 0.4° is accepted; for an axial distance up to ± 0.14 cm from the center, an axial divergence up to ± 3.5° is accepted. This matches by design the size of the beam spot on the polarizer seen by the system (± 0.5 cm radially by ± 0.1 cm axially) and limits the geometrical scattering angle from calcium to 25.5° ± 0.4°.

The general results of the optics study were confident predictions of the energy resolution, beam intensity, spot size, and angular divergence, all of which indicated that the inelastic asymmetry experiment was feasible. The beam equipment (magnets, slits, and vacuum equipment) was assembled and surveyed into position, and power supplies and water cooling were provided for the analyzer and Q12. The predicted beam properties were found immediately with the predicted magnetic field settings, and these results were then found to be essentially optimum. The predictability of the secondary optics system, its insensitivity to cyclotron beam conditions or to small variations in focusing the primary optics, seems to be due to the fact that the secondary

system forms its own beam. It accepts and acts upon a certain portion of the beam scattered from the polarizer, and this portion is not strongly influenced by the beam conditions upstream.

The performance of the secondary optics system for a typical value of 18 μA of 50-MeV protons on the calcium polarizer is as follows. A polarized beam of 40-MeV protons is accepted and rendered parallel by lens Q6 and is then (radially) focused by lens Q7 to a spot about 0.5 cm wide by 3 cm high at the object slit of the analyzer magnet. The intensity at that point is about 7×10^8 protons/sec. A beam of about 2×10^8 protons/sec gets through the object slit (0.42 cm wide by 2.54 cm high) and the shielding baffle (2.03 cm wide by 2.54 cm high). This is analyzed by the magnet and double-focused at the image slit (0.42 cm wide by 2.03 cm high). A 10^8 proton/sec beam emerges from this slit with an energy spread of 500 keV. This propagates through Q12 without loss in intensity and is focused to a spot 0.4 cm wide by 1.1 cm high at the target. The beam there has a maximum angular divergence of about ± 2° in the scattering plane and ± 1° in the vertical plane. Using object and image slits which are 0.25 cm wide, a 300-keV beam may also be produced which has approximately the same spot size and angular divergence at the target and an intensity of about 5×10^7 protons/sec.

In routine use, it has proved desirable to optimize empirically the middle element of quadrupole Q12 to achieve the sharpest focus at the target. This, however, cannot be done at these low intensity levels by the familiar practice of placing scintillating material in the beam, to be viewed remotely. In this case we first located the beam in the scattering chamber by exposing Polaroid film placed behind cross hairs at the target position. A slit was then installed at the target position whose aperture approximates the optimum spot size. With an ionization chamber placed behind the slit, the quadrupole was easily focused by maximizing the beam passed through the aperture. The resultant spot size and centering was then checked by removing the slit and exposing Polaroid film again at the target position. This method of focusing depends on good alignment of the quadrupole Q12, so that variations in its excitation will not steer the beam away from the center of the slit. Other techniques used routinely to fix the position and direction of the beam at the target are described below.

B. Measurement of Beam Polarization

We turn now to the determination of the beam's polarization, which must be accurately known in order to normalize the asymmetry measurements. The polarizations

measured in the elastic scattering work with the α-p produced beam were determined by

$$P(\theta) = A(\theta)/P_B \quad , \tag{1}$$

where P is the polarization (polarizing power) of the target, P_B the magnitude of the beam polarization, and A the measured left-right asymmetry* in the scattering:

$$A(\theta) = \frac{N_L(\theta) - N_R(\theta)}{N_L(\theta) + N_R(\theta)} \quad . \tag{2}$$

Here N_L is the number of protons scattered to the left, and N_R the number scattered to the right, with left defined such that $\underset{\sim}{k}_i \times \underset{\sim}{k}_f$ is in the direction of the beam polarization (Basel convention). The direction of the beam polarization was known from the p + ^{4}He data,[31] and its magnitude was determined by performing[20,29] a double-scattering experiment for Ca at 25.5°. The latter gave the magnitude of the Ca polarization from $P = \sqrt{A}$, so that P_B for the α-p beam could be found from the observed asymmetry it produced in Ca scattering, through Eq. (1). The α-p beam polarization, in turn, determined the polarization of the other targets whose asymmetries were measured (^{12}C, ^{90}Zr, ^{208}Pb). In

---

*We distinguish between the observed asymmetry A and the quantity ϵ, which will be used to denote the asymmetry produced with a completely polarized beam, $\epsilon = A/P_B$.

particular, both the polarization and differential cross section for ^{12}C were sizable and yet slowly varying functions of angle near 60° for 40-MeV protons. When both the thin and thick calcium targets were later used as polarizers, in place of the α-p scattering, the beam polarization produced by calcium scattering could be determined and checked routinely by the ^{12}C asymmetry observed at 60°, using Eq. (1) and the known sign and magnitude of the ^{12}C polarization.

This chain of measurements, however, still resulted in a rather unsatisfactory knowledge of the ^{12}C polarization and, consequently, of the beam polarization produced by the thick calcium polarizer. The weakest link was due to the difficulty of performing a double-scattering experiment at 25.5° for Ca, where the rapid variation of both the cross section and polarization required a very tedious alignment procedure. The experiment was done a number of times, but the polarization could not be reproduced to better than $\Delta P/P \simeq \pm 8\%$. There were other problems with the double-scattering measurement which involved the matching of angular acceptances and energies in the first and second scatterings, and these effects could be accounted for only by fairly indirect calculations. The net result was that all of the asymmetries measured at that time could be normalized with the value of P_B only to within about ± 10%.

It then came to our attention that a very good measurement had been made[39] at 27.5 MeV of the absolute elastic polarization for ^{12}C at 65° lab. At this angle, the cross section and polarization are slowly varying functions of angle at both 27.5 MeV and 40 MeV, and alignment uncertainties present no problems. The 40-MeV beam was degraded to 27.5 MeV by placing an aluminum absorber in front of the scattering chamber; we could then determine the beam polarization by measuring the ^{12}C asymmetry at 65° and by using its known[39] polarization. This gave the polarization of our 40-MeV beam to be 27.4 ± 0.5 percent, where the uncertainty includes both our uncertainty in the asymmetry measurement and the quoted[39] uncertainty in the 27.5-MeV data. By removing the absorber and measuring the ^{12}C asymmetry at 40 MeV, we then had also a well-known absolute polarization for ^{12}C at that energy. The result for 40-MeV protons on ^{12}C at 65° lab is P = 70.8 ± 1.8 percent. The ^{12}C target was thereafter used as an analyzer in order to check the beam polarization in the different runs which comprise this work. This was desirable on grounds of the general complexity of our system, but in fact the beam polarization was never found to change.

The beam polarization value of 27.4 percent was actually quite close to the previous result of 28 percent, which depended on the double-scattering experiments. But the

improvement in the uncertainty, $\Delta P_B/P_B = \pm 1.8\%$ as opposed to $\pm$ 10%, represents a considerable gain in the accuracy of our measurements. The only unmeasured complication in the new determination of P_B is the assumption that the beam is not significantly depolarized by attentuating its energy from 40 MeV to 27.5 MeV. This assumption is theoretically[40] justified, and no experimental depolarizations have been detected for large proton energy attenuations.[41] We note finally that we have also found the asymmetry from ^{12}C at 65° to be constant, within our uncertainties, for proton energies from 26.9 MeV to 28.5 MeV, so that it was not necessary to match exactly the energy of 27.5 MeV. These proton energies were determined to within $\pm$ 0.2 MeV by measuring the residual range in an emulsion.

2. Data Acquisition

A. Counting Equipment

The present asymmetry measurements were made with the scattering chamber, counter array, and electronics equipment[29] used for the previous elastic scattering work.[20] The chamber is 17 inches in diameter and is made of stainless steel. A 1.25-inch slot for the scattered particles extends around the circumference from about 5° to 175° on each side of the beam and is vacuum sealed by a 2-mil thick Mylar window. The chamber is open to vacuum at the front, where

the beam enters, and is closed off by an aluminum foil at the end of a 10-inch snout which protrudes from the back. The beam passes through this foil and into a Faraday cup. The chamber is mounted on a support with adjustments for elevation, horizontal position, horizontal rotation, and for tilting the plane of scattering. These are all adjusted prior to each run by surveying, so that the chamber is properly oriented with respect to the incoming beam. At the center of the chamber is a multiple-target holder which permits a given target to be selected remotely. Its tilt relative to the beam direction can also be adjusted without breaking vacuum.

Outside the chamber (and outside the vacuum envelope) two semi-circular collimator mounts are attached to the support structure, one on each side of the beam. Each mount has 16 grooved openings which hold 0.125-inch thick brass collimators with apertures spaced $10° \pm 0.05°$ apart. The collimators are about one inch away from the Mylar window on the chamber. The counter assemblies are also attached to the collimator mounts, with each counter placed directly behind a collimator. Each bank of collimators can be independently rotated at a radius of 9.375 inches from the center of the chamber, allowing the angular range between 8° and 172° to be covered on each side of the beam. The angular position of the collimator openings (the counter

apertures) can be set with this apparatus to within ± 0.05°. The maximum variation of the aperture area in a set of 32 collimators is ± 1 percent.

Thirty-two NaI(Tl)-photomultiplier counters were used to detect the scattered protons. Each of these consists of a 1-inch diameter by 3/4-inch-thick crystal pack* mounted with a high-viscosity silicone fluid** to an RCA 6199 phototube. These tubes were selected prior to their use in the array by requiring the NaI-phototube resolution to be 10% FWHM or better for ^{137}Cs γ-rays. Two sizes of collimator apertures were used; one was 0.125 inches in diameter and the other was 0.375 inches wide by 0.75 inches high. For the small apertures, the resolutions of the 32 counters for 40-MeV protons vary from about 300 keV to 500 keV. For the large apertures (but same counting rate) the resolutions are between about 450 keV and 650 keV. The small apertures have an area 22.6 times smaller than the large apertures, but could be used at forward angles for some of the inelastic asymmetry measurements where the smaller count rate could be tolerated.

An electronics network routes the 32 photomultiplier outputs to a 20,000-channel pulse-height analyzer*** whose

---

*Harshaw Chemical Company, Cleveland, Ohio.

**"200 Fluid", Dow Corning Corporation, Midland, Michigan.

***"Tullamore Model MP 204 RT Multiparameter Analyzer", Victoreen Instrument Company, Cleveland, Ohio.

memory configuration is used in a 50 x 400 mode, effectively as thirty-two 400-channel analyzers. Each photomultiplier tube is connected at its anode to a variable-gain preamplifier, and the 32 preamplifiers are fed to the analyzer X-ADC through a single linear amplifier. Identifying pulses from a Schmidt-trigger discriminator in each preamplifier are converted to a binary-coded-decimal Y-address signal for the analyzer by a passive diode matrix. Each discriminator threshold was commonly set at a value corresponding to a proton energy about 20 MeV below that of the elastically scattered protons. The X-ADC is gated by the trigger pulses which are, in turn, gated in anticoincidence by a busy signal from the analyzer. The net result is that the photomultiplier pulses for protons of energy greater than about 20 MeV are stored in one of the 400 X-channels according to their pulse height (proton energy) and in one of 32 Y-channels according to the counter from which they originated. The analyzer memory is read out onto magnetic tape, and 20,000 channels of data are dumped in approximately fourteen seconds.

Some typical energy spectra are shown in Fig. 2. With an energy spread in the beam of 500 keV, and with the larger counter collimators, the overall resolution is about 750 keV FWHM at forward angles. The targets used were in the range 20 to 30 mg/cm^2 in thickness, and at back angles the overall resolution is increased to about 1 MeV due to the passage

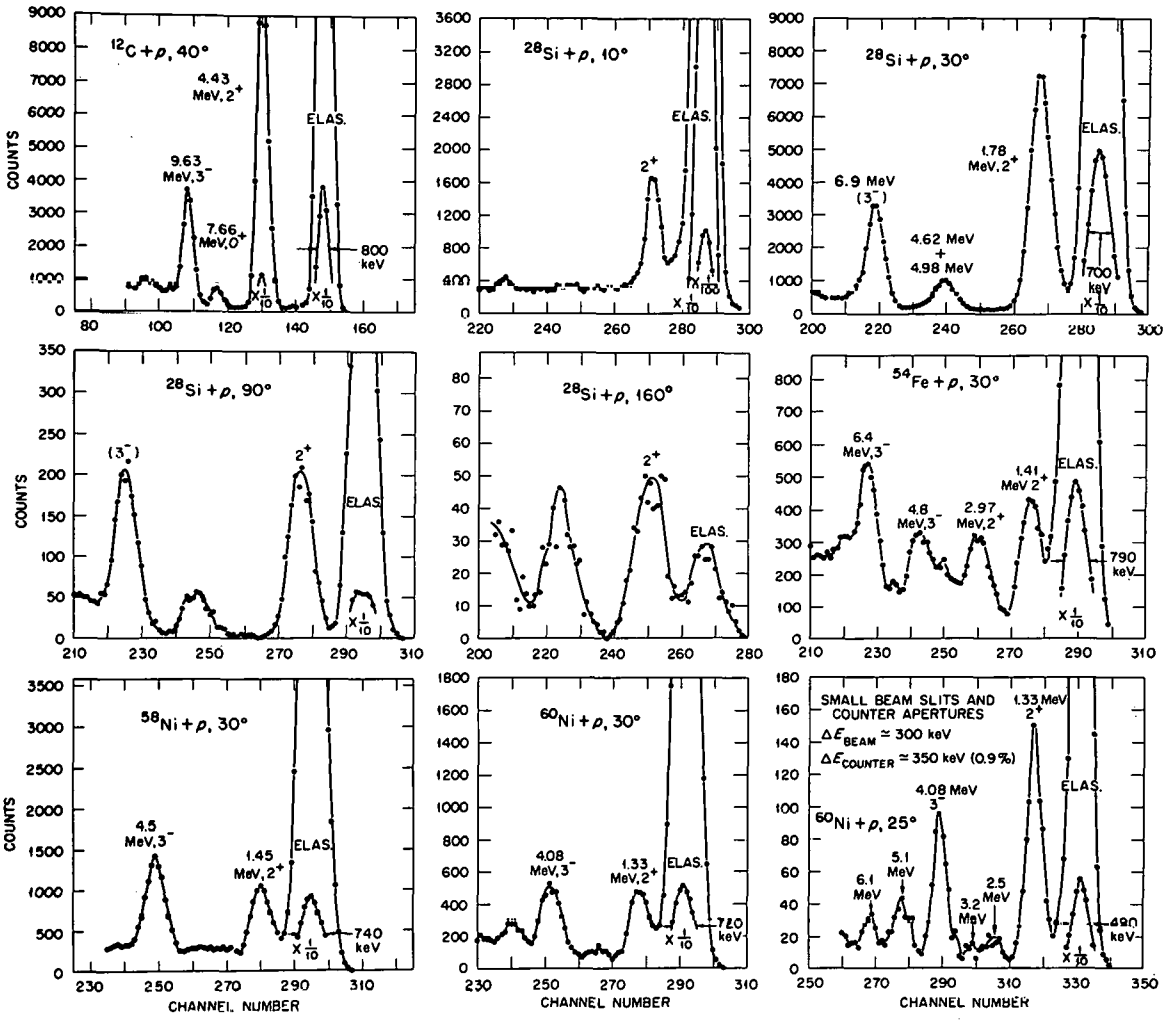

Figure 2. Energy spectra. Proton spectra at various angles are shown for the different targets. These have an overall resolution of about 750 keV achieved using the larger magnet slits and counter collimators discussed in the text. Also shown for ^{60}Ni is a spectrum with improved resolution achieved by stopping down the slits and collimators.

of the scattered beam back through the target. However, at back angles the intensity of the elastic proton group is comparable to that of the inelastic groups, and the first excited state need not be so well separated in order to resolve it from the elastic peak. Also shown for ^{60}Ni is a spectrum taken with a beam spread of 300 keV and with the smaller counter aperture. This results in an overall resolution of about 500 keV FWHM at forward angles, but the counting rate is decreased by a factor of about forty.

B. Targets

The ^{28}Si target was made of natural (92.21 percent ^{28}Si) high-purity silicon and was 32.1 mg/cm^2 thick. The ^{54}Fe target was 97.4 percent enriched and 18.0 mg/cm^2 thick. Nickel-58 was 99.95 percent enriched and 29.95 mg/cm^2 thick, and ^{60}Ni was 99.1 percent enriched and 19.7 mg/cm^2 thick. The targets were all about 2 inches tall by 3/4 inch wide, and their thickness at the center (where the beam is focused) could not be confidently deduced from the total weight and area of the foil. In order to normalize the cross section measurements, thin targets (about 5 mg/cm^2) of ^{54}Fe, ^{58}Ni, and ^{60}Ni were also used to measure the elastic scattering. The thickness values given above were deduced from these measurements and pertain to the centers of the thick targets. The thicknesses of the

thin targets at their centers were determined by scanning them with a collimated, 5.48-MeV, alpha-particle beam from ^{241}Am and measuring the energy attenuation with a solid-state counter. The average of these alpha thickness values measured over the entire surface of each thin target was also compared to its weight-area thickness value and found to agree within the estimated accuracy of the alpha measurements, which was ± 5 percent. The thick Si target was destroyed, and its thickness was obtained directly by measuring the weight and area of the fragments. The thicknesses of the fragments near the center were found to be the same within two percent. The precision of the thickness measurement is assigned to be ± 5 percent for all targets.

C. Running Procedures

We turn now to the procedures used routinely to accumulate the asymmetry and cross-section data. The beam is first focused and centered in the scattering chamber in the manner described in the previous section. The energy of the secondary beam is then determined by scattering from ^{208}Pb and measuring the pulse-height variation of the elastic peak for different thicknesses of Al absorber placed before a counter at 10°. In each run the energy was also measured by residual range in emulsion, and a

comparison of the two methods revealed a constant difference of about 1 MeV. Comparison with a magnetic rigidity measurement, good to 0.5 percent in energy, confirmed the correctness of the emulsion method. Although the source of error in the pulse-height method is not understood, this method has proved to be consistent; and the speed and ease of the pulse-height method were essential in setting the cyclotron frequency at the beginning of each of the three different experiment periods that were used for this work. As a result of these energy measurements, we can state that all of the asymmetry and cross section data presented here were taken with protons of energy 40.0 ± 0.4 MeV. When it was necessary to change the cyclotron frequency to attain the correct energy, the focusing and centering procedure was repeated after the energy change. The constancy of the energy after its initial setting is verified by the constant field of the analyzing magnet maintained during the runs.

The angular alignment of the counter banks on each side of the beam was then checked by positioning the most forward counters at 10° on both the left and right sides and observing the asymmetry in the elastic scattering from ^{208}Pb. Assuming the scattering to be purely Coulomb, a ± 0.1° misalignment of the counters relative to the average beam direction produces an 8 percent departure from unity

of the ratio $N_L(10°)/N_R(10°)$, using the notation of Eq. (2). The position of each counter array can therefore be quickly adjusted to agree with the beam direction to within ± 0.05°. The alignment was checked in this way before and after each individual asymmetry run (each accumulation of data) and was never found to differ by more than this amount, ± 0.05°. During a run, the position and alignment of the beam were monitored with a split ionization chamber located at the exit of the scattering chamber, in front of the Faraday cup. This is sensitive to a 10-mil transverse displacement of the chamber from its correct position and is, conversely, a sensitive monitor of the constancy of the beam geometry during the run. As mentioned previously, ^{12}C data were taken during each group of asymmetry runs in order to check the polarization of the beam.

Our method of aligning the beam depends on the assumption that elastic scattering from Pb at 10° gives a small polarization, and not that the scattering is exactly Coulomb. Our measurement[21] for Pb is actually $\sigma(10°) \simeq 0.8\ \sigma_R(10°)$, where $\sigma_R(\theta)$ is the Coulomb differential cross section. However, we also know[21] that $\sigma(\theta)$ near $\theta = 10°$ falls off at least as fast as $\sigma_R(\theta)$ with increasing θ, and that $P(\theta)$ is slowly varying. Assuming the scattering to each side of the beam decreases with θ like Coulomb scattering, $N(\theta) \sim \sin^{-4}(\theta/2)$, but that there exists a finite polarization

$P(\theta)$, then from Eqs. (1) and (2) we find that the amount of offset $\Delta\theta$ needed to produce $N_L(\theta + \Delta\theta) = N_R(\theta - \Delta\theta)$ is $\Delta\theta \simeq (1/2)P_B P(\theta)\sin(\theta/2)$. Thus, even if the polarization from Pb at 10° were as high as 5 percent, a misalignment of only $\Delta\theta \simeq 0.03°$ would be introduced by setting the counter angles to produce no observed asymmetry.

The asymmetry data for the four targets were taken at 5° intervals, generally over the range 10° to 165°. Elastic and inelastic data were obtained simultaneously. The runs for each target were broken down in two ways, depending on whether or not satisfactory resolution could be achieved near 90° for protons reflected back out of the target when it was tilted at an angle of 45°. The reflection geometry was satisfactory for ^{28}Si, ^{54}Fe, and ^{60}Ni; and the range could be covered in four runs, lasting about six hours each, with two runs having a target tilt of 0° (normal to the beam) and two for a target tilt of 45°. For each tilt, two runs were taken, one with the counter banks (both left and right) set to cover the angles 10°, 20°,..., 160° and the other run to cover the angles 15°, 25°,..., 165°. The runs made with a tilt of 45° cover the region from 65° to 115°, which are obscured by the target shadow in the runs taken with a 0° tilt. The small collimators (1/8-inch diameter) were used at forward angles out to an angle where the number of counts in the inelastic groups would be comparable to that obtained at the back angles where the large collimators (3/8 inch by 3/4 inch) were used.

The reflection geometry was unsatisfactory for the ^{58}Ni target (30 mg/cm^2), but the data for this nucleus could also be obtained in four runs. Two runs were made at the angles 10°,..., 160°, one with a tilt of 45° in one direction and the second with a tilt of 45° in the opposite direction. The other two runs were made for these two target tilts at the angles 15°,..., 165°. In this procedure, the data at forward and back angles for scattering to the left come from a different run than those for scattering to the right. But the data near 90° are repeated, so that the relative angular distributions on each side of the beam can be inter-normalized at 5 angles around 90°. Integration of the beam current is not required but served as a check on the normalizations.

Extra asymmetry data were taken for the targets ^{28}Si and ^{60}Ni to optimize the energy resolution at forward angles by using exclusively the smaller collimators. These data for ^{28}Si extend from 10° to 67.5° in 2.5° intervals, and for ^{60}Ni from 20° to 65° in 5° intervals. The improved resolution reduced the uncertainties in this region by about 50 percent.

While the asymmetry runs yielded cross-section information by averaging the counts for scattering to the left and right, better elastic cross-section data, and some inelastic data at forward angles, could be easily obtained

by using the counter array in the direct, unpolarized beam. There, the beam spread is lower, about 250 keV, and the intensity copious; so that the smaller counter collimators could be used out to back angles, and the data could be taken at smaller intervals. The overall angular resolution is also improved from ± 2.5° to ± 1°. This was done for all four targets by moving the scattering chamber to another beam line in the same experiment area. For these measurements, the counters to the left of the beam are set at different angles than those to the right. A "normalization run" was first taken at low beam intensity, with an analyzer dead time of less than one percent, which covered 12 angles in the forward hemisphere. For ^{54}Fe, ^{58}Ni, and ^{60}Ni, the mentioned "thin" targets were used for this purpose. The rest of the runs, about 8 per nucleus, could then be made with the thick targets and at higher beam levels (an analyzer dead time of about five percent) by normalizing the relative cross sections to the elastic data obtained in the normalization run. Various combinations of target tilts and angle settings of the counter banks were used in a way to minimize the total time necessary to accumulate the elastic and inelastic angular distributions. When data were taken at back angles, it was more efficient to cover the counters out to about 25° to eliminate their contributions

to the analyzer dead time. Typically, elastic cross-section data from 10° to 170° in 2.5° intervals, and inelastic cross-section data from 20° to 70° in 5° intervals, could be obtained for a target in about 12 hours.

At the end of the asymmetry and cross-section runs, a pulser calibration of the electronics was made at the existing gain levels for several counters by varying the voltage of pulses applied to the input of their pre-amplifiers. Assuming the photomultiplier tubes to be linear, the energies of the inelastic groups observed in the spectra could then be established relative to the elastic groups and, through kinematics, the Q values thereby determined. By doing this for many counters, however, this procedure was found to be reproducible only to about ± 200 keV. Within this margin, we are in agreement with the energies for the levels we observe which are given in Nuclear Data Sheets and with those determined by Stovall and Hintz.[42] We use these two sources to name the states, except for the excitation we observe near 6.9 MeV in ^{28}Si, which we only tentatively identify as the known octupole excitation at 6.88 MeV.

3. Data Reduction

A. Peak Integration

The data on magnetic tape from the pulse-height analyzer were processed with a CDC 160-A computer. A program SLAP[43] was used to plot the number of counts versus proton energy (X channel number) for each counter (Y channel number). The program also prints out the number of counts and a running (accumulated) sum of counts along the energy axis. In order to unfold the spectra carefully in the region of the tails of the elastic and inelastic proton peaks, a semi-logarithmic plot of the spectra was more useful. These automatic plots were an invaluable aid in unfolding the 2000-odd peaks which were reduced for these measurements.

The SLAP plots were unfolded by hand in the manner illustrated for a ^{60}Ni spectrum in Fig. 3. By examining a large number of spectra from different counters for ^{12}C, where the elastic and inelastic peaks are well separated, it was established that the elastic peak-shape (in a semi-logarithmic plot) is consistently and precisely repeated in the inelastic peaks. Consequently, the elastic peak-shape could be used to unfold the inelastic peaks by successive approximations. The first step is illustrated on the left-hand side of Fig. 3 and consists of drawing the elastic peak-shape, near its maximum and on its high-energy side, through the

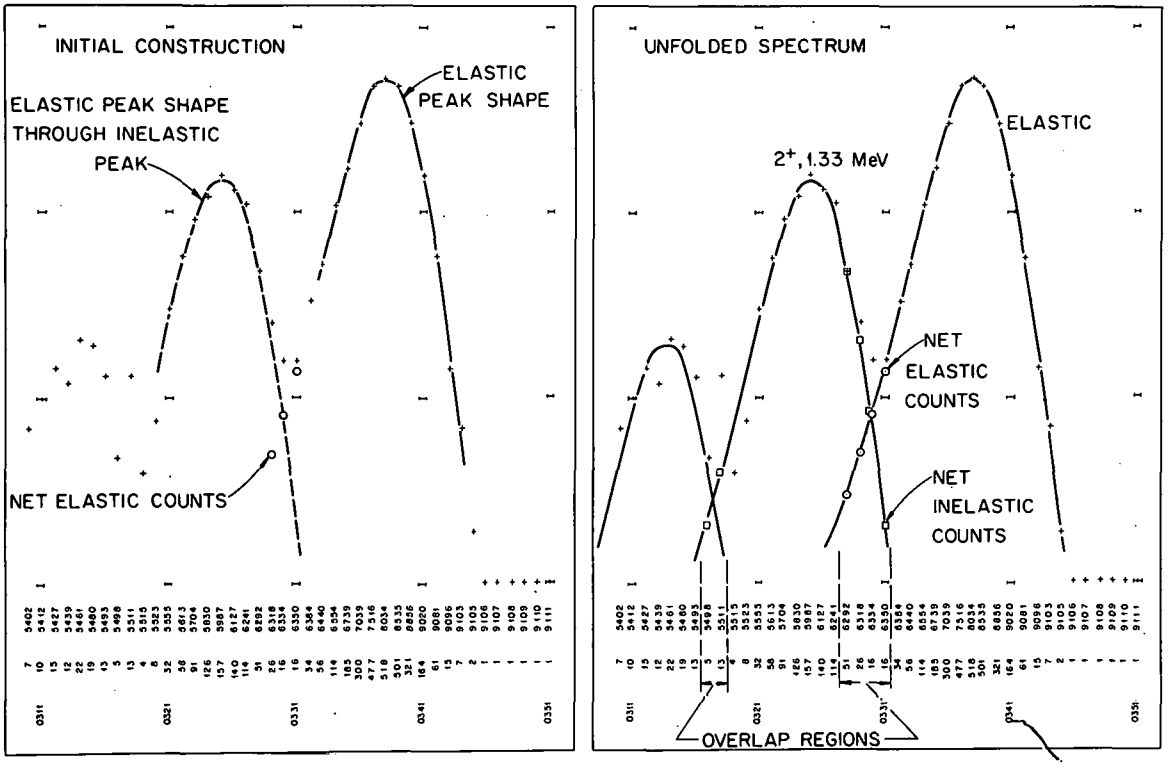

Figure 3. Reduction of energy spectra. Two copies of the same ^{60}Ni spectrum at 25°, as displayed by the plot program SLAP, are shown to illustrate the unfolding procedure described in the text. The crosses in the computer output are the points in a semi-logarithmic plot of the total counts per channel versus channel number. Along the energy axis are listed, from bottom to top, the channel number, the counts per channel, and a running sum of the counts per channel. A number identifying the counter from which the spectrum originates is printed near channel zero (not shown above).

inelastic points. This first approximation to the inelastic contribution is then subtracted from the total counts near the low-energy side of the elastic peak to obtain the net elastic contribution in that region. The elastic peak-shape is then extended smoothly to lower energies, and a second approximation to the net inelastic counts near the maximum of the inelastic peak is obtained by subtracting the new elastic points from the total counts. The process is continued until the two unfolded peaks agree in shape and account for the total counts observed, within statistics and in view of other nearby groups which are not resolved. No significant elastic peaks from contaminants were observed in these spectra taken with thick (20-30 mg/cm^2) targets. The unfolded spectrum for ^{60}Ni is shown on the right in Fig. 3, with lines drawn through the net elastic contribution and that from the first excited state. Higher excited states are reduced using the unfolded elastic peak-shape. Except for the regions of overlapping peaks, a peak may be quickly integrated by subtracting the printed value of the accumulated counts at its low-energy end from the value at its high-energy end. To this is added the peak's net contribution in the regions of overlap, as deduced by this method of construction.

B. Compilation of Results

Relative elastic and inelastic cross sections for each target were obtained from the asymmetry runs by averaging (summing) the net, unfolded counts in the proton groups scattered to each side of the beam. The relative elastic cross sections from the various "cross-section runs" for each target, the runs made separately with the unpolarized beam, all have several angles in common with each other. These "runs" are taken with different counter-angle settings and have different amounts of bombardment and target tilts, so that they have different normalizations. The cross-section runs were inter-normalized at their common angles, with greater weight given to angles where the cross section is slowly varying; and a composite relative cross section was thus formed from these data. Using the relative elastic cross sections deduced from the asymmetry data, the normalization of the inelastic cross sections obtained from the asymmetry runs was then determined relative to this composite elastic cross section. Some inelastic data from the cross-section runs were used to augment the data from the asymmetry runs. The elastic cross-section data from the asymmetry runs, however, were used solely to normalize the inelastic cross sections to the elastic data. This and other redundancies in the elastic and inelastic data, taken at different times and in different ways, afforded a considerable number of consistency checks for these measurements.

There was one exception to this procedure for normalizing the inelastic cross sections to the relative elastic angular distribution. The effect of isotopic impurities in the elastic data requires no correction since (i) the elastic contributions from neighboring isotopes are not resolved, (ii) the cross sections are nearly identical, and (iii) since the amount of impurity is small. A similar situation exists for the inelastic groups measured in ^{54}Fe, ^{58}Ni, and ^{60}Ni, primarily because of the high isotopic purity of the targets. The natural Si target, however, contains 4.7% ^{29}Si and 3.09% ^{30}Si, both of which have excited states which make an uncertain contribution to the observed proton groups corresponding to the 1.78-MeV and 6.9-MeV excitations in ^{28}Si. The normalization of the inelastic data for ^{28}Si was therefore increased by a factor of 1.039, which is half way between assuming no inelastic contributions from the adjacent isotopes and, conversely, assuming all the isotopes have a state at the same energy with equal strength. Neither situation is true, but an additional normalization uncertainty of ± 4% is added for the inelastic cross section data from ^{28}Si to bracket these extremes.

The relative elastic cross sections for each target were then normalized to the absolute elastic data obtained in the mentioned "normalization runs", and this in turn determined the absolute normalization for the inelastic cross sections. The absolute elastic cross-section data were deduced from the

known target thickness t, in units of the number of nuclei per unit area; the integrated beam current N_{tot}, expressed as the number of incident protons; the solid angle of the counters $\Delta\Omega$; and the observed number of counts $N(\theta)$: $(d\sigma/d\Omega)_{lab} = N(\theta)/(N_{tot}\, t\, \Delta\Omega)$. The absolute cross sections were corrected by a factor of 1.023 to account for the loss of counts due to reactions undergone by the scattered protons in the NaI crystal. This factor was deduced from the work of Measday[44] for our method of unfolding the proton spectra, in which we do not include the "tails" of the peaks below about 1 MeV from their maxima. Finally, the absolute elastic and inelastic cross sections were converted to the center-of-mass system by multiplying them by the appropriate relativistic Jacobian.

The elastic and inelastic asymmetry results $\epsilon(\theta)$ are normalized to 100-percent beam polarization using

$$\epsilon(\theta) = \frac{1}{P_B} \frac{N_L(\theta) - N_R(\theta)}{N_L(\theta) + N_R(\theta)} , \qquad (3)$$

where for the elastic data $\epsilon(\theta) = P(\theta)$. Again, $N_L(\theta)$ and $N_R(\theta)$ are the net number of counts in the proton peaks on each side of the beam, using the Basel convention; and the beam polarization P_B is 0.274.

C. Error Analysis

The total absolute error in the normalization of the cross-section data is taken to be an uncorrelated combination of the uncertainty in target thickness (± 5%); solid angle (± 1%); beam integration (± 2%); and, for the inelastic results for ^{28}Si, the contributions from isotopic impurities (± 4%). The absolute error for the elastic cross sections, and for the inelastic cross sections for Fe and Ni, is then ± 5.5%, and that for the inelastic Si data is ± 6.8%. The absolute error in the normalization of the asymmetries is taken to be that due to the uncertainty in beam polarization, ± 1.8% of the value of ϵ.

The relative probable errors in the cross section and asymmetry data stem mainly from uncertainties in unfolding the energy spectra and from statistics. These are assumed uncorrelated, so that the total error ± ΔN in the net counts in a peak is given[45] by

$$\Delta N^2 = \Delta N_0^2 + \Delta N_B^2 + \Delta N_S^2 \quad . \tag{4}$$

ΔN_0 is the estimated uncertainty of the counts assigned to the peak in the region where it overlaps adjacent peaks; ΔN_B is the uncertainty in any background under an inelastic peak due to the tail of the elastic peak; and ΔN_S is the total statistical error. Typically, ΔN_0 was judged

to be about 30% of the total contribution to the peak in an overlapping region; and ΔN_B amounted to about 20% of the total background under the peak (i.e., subtracted from it). ΔN_B was a major contribution to the errors for the inelastic data at angles less than about 50°. The number of counts obtained in the inelastic peaks during the asymmetry runs was usually 500 or more, so that the fractional statistical error in the relative inelastic cross sections $(N_L + N_R)$ was $\sim 4\%$ or less; and the statistical error in the asymmetry was $\Delta\epsilon \lesssim 0.12$, depending on the value of ϵ. The peak-unfolding errors ΔN_0 and ΔN_B make similar contributions to the inelastic errors except at angles less than about 50°, where they are largest. The relative errors for the elastic data are mainly due to statistics.

The total fractional relative error $\pm \Delta\sigma/\sigma$ in the differential cross section at each angle is then $\pm \Delta N/N$ where ΔN is given by Eq. (4) or, when the data come from an asymmetry run where $\sigma = \text{const.}\ (N_L + \eta N_R)$,

$$\frac{\Delta\sigma}{\sigma} = \frac{\left(\Delta N_L^2 + \eta^2\, \Delta N_R^2\right)^{1/2}}{N_L + \eta\, N_R} \quad . \tag{5}$$

ΔN_L and ΔN_R are each given by Eq. (4), and η is the ratio of the normalizations of N_L and N_R, in case they were taken in different runs (as for the data from ^{58}Ni). Using Eq. (3),

the errors ± ΔN propagate[45] in the asymmetry measurements to produce an error ± Δε given by

$$\Delta\epsilon^2 = \frac{\eta^2}{P_B^2}\left\{\left[\frac{2N_R\,\Delta N_L}{(N_L + \eta\, N_R)^2}\right]^2 + \left[\frac{2N_L\,\Delta N_R}{(N_L + \eta\, N_R)^2}\right]^2\right\}. \quad (6)$$

To handle the fairly large volume of elastic and inelastic data accumulated in the asymmetry runs, a program was written[46] to compute the relative cross sections, the asymmetries, the relative errors due separately to statistics and peak unfolding, and the total relative errors given by Eqs. (4), (5), and (6). The input data were the net counts in each peak, estimates of the unfolding errors, the beam polarization, and for ^{58}Ni the normalization factor deduced by comparing the runs at their common angles near 90°.

Two other uncertainties are recognized but not included in the probable error evaluated for each datum. Maximum beam-alignment uncertainties are estimated to be equivalent to a ± 0.1° error in the average direction of the beam relative to the counters. The amount of spurious asymmetry this introduces in the elastic and inelastic data depends on the actual asymmetry, the beam polarization, and the variation of the asymmetry and cross section with angle. For Coulomb scattering with $\epsilon = 0$ we have on either side of the beam $N(\theta) \sim \sin^{-4}(\theta/2)$, so that the spurious asymmetry

$\epsilon'(\theta) = (1/P_B)[N_L(\theta - \Delta\theta) - N_R(\theta + \Delta\theta)]/[N_L(\theta - \Delta\theta) + N_R(\theta + \Delta\theta)]$ produced by a misalignment in the beam direction of an amount $\Delta\theta$ toward the left is approximately $\epsilon'(\theta) = 2\Delta\theta/P_B \sin(\theta/2)$. For a 0.1° misalignment and our beam polarization of 27.4%, this gives a spurious asymmetry of $\epsilon' = 0.14$ at 10°, 0.09 at 15°, and so forth. The angular distribution of protons inelastically scattered to either side of the beam changes at a slower rate than Coulomb scattering at 15° (smaller $N'(\theta)/N(\theta)$), and the effect of misalignment is correspondingly less. We estimate a maximum misalignment error in the inelastic asymmetry data of $\Delta\epsilon = 0.03$.

The other error is due to the overall angular resolution, which was ± 2.5° in the asymmetry runs and ± 1° in the cross-section runs. These angular spreads correspond to an uncorrelated addition of the maximum divergence in the beam and of the angular acceptance of the counter collimators, including the effect of the finite size of the beam spot on the target. Estimates of the effect of multiple scattering in the targets were found to be negligible. The errors due to angular resolution are everywhere negligible (relative to other uncertainties) for the inelastic cross sections, and are significant for the elastic cross sections only around their deep minima near 20° for Fe and Ni and, to a lesser extent, near 35° for Si. This was ascertained by comparing the

elastic data obtained in the asymmetry runs to those obtained in the cross-section runs. The former, with 2.5 times the angular acceptance, agree excellently with the latter except for these angular regions, where the data from the asymmetry runs are too high due to averaging over the sharp minimum. The total relative errors for the elastic cross-section data, which were all taken with a ± 1° angular spread, were arbitrarily increased in these regions to ± 10% for Fe and Ni and to ± 5% for Si.

The effect of the ± 2.5° angular resolution on the elastic and inelastic asymmetry measurements seems smaller than might be expected at first glance. Optical-model predictions of the present elastic polarizations have been made using various reasonable sets of parameters, including those which fit other polarization data taken with better angular definition. When any of these predictions are averaged over a ± 2.5° acceptance, important differences occur only at the sharp oscillation between 20° and 30° in Fe and Ni. The total relative errors there were increased to $\Delta\epsilon = 0.05$. At other angles, our elastic polarization data show a more gentle variation with angle for which the present angular spread should be satisfactory. The oscillations observed in the inelastic asymmetries rise gently to maximum values near $\epsilon = +1$, and fall at a comparable rate to minima near $\epsilon = 0$. It therefore seems that the only

behavior of the inelastic asymmetries which could be obscured by the spread of ± 2.5° would be a rather unlikely, negative "spike" near the minima in their angular distributions.

4. Results

Tables of the elastic and inelastic cross-section and asymmetry data and their total relative errors as defined above are given in Section VII. Plots of all of the data appear in the next Section along with calculated curves.

A. Cross Sections

The elastic cross sections for ^{54}Fe, ^{58}Ni, and ^{60}Ni have been measured previously[47] out to about 120° with 40-MeV protons at Minnesota. Our cross section for ^{54}Fe appears to agree well with those data out to about 50°, but thereafter is about 10% lower than the previous results. The data for ^{58}Ni compare in the same way out to about 90°, but at larger angles our results are about 20% lower. Our elastic cross section data for ^{60}Ni seem to agree well with the previous data out to 100°.

The inelastic cross sections for iron and nickel have also been measured[42] with 40-MeV protons at Minnesota. These were normalized to the previous[47] Minnesota elastic data. They extend to 90° and were taken with an energy resolution comparable to that for the present measurements.

Their agreement with the present data for the four transitions in ^{54}Fe is rather poor. The present cross sections become increasingly higher than the previous values as the angle is reduced, and the discrepancies are larger for proton groups closer in energy to the elastic peak. At 20°, our cross section is about 20% higher for the state at 6.4 MeV, 50% higher for the states at 4.8 MeV and 2.97 MeV, and nearly a factor of two higher for the 1.41-MeV transition. At 50° the discrepancy is about 10% at 6.4 MeV, 35% at 4.8 and 2.97 MeV, and 45% at 1.41 MeV. However, the results do generally agree within their estimated uncertainties. In the previous work the energy spectra were unfolded in a way which assumed a maximum contribution from the general background of unresolved nearby peaks, and the quoted uncertainties are asymmetric. The data past 15° for the 2.97-MeV excitation in ^{54}Fe, for example, have an uncertainty of +35% and -5%. Our method of unfolding the spectra involves more of an average of the maximum and minimum possible contributions, and this difference can account for the discrepancies in the ^{54}Fe data.

Our agreement with the previous Minnesota cross-section data for the two states in ^{58}Ni seems quite good except for the 1.45-MeV transition at angles less than 20°. There, the previous data are higher than the present results by almost a factor of two. The opposite appears to

be true of the inelastic cross section for ^{60}Ni, where our data for the first excited state is about a factor of two higher at the most forward angles. Elsewhere the data for both transitions in ^{60}Ni are also in good agreement with previous values. These differences for the first-excited states at angles less than 20° are readily explained by systematic errors in either or both experiments in judging the contribution from the elastic peak.

The better agreement at larger angles between previous and present 40-MeV results for the inelastic cross sections for ^{58}Ni and ^{60}Ni than those for ^{54}Fe is consistent with the different manner in which the spectra were reduced. There are four states (those measured) of comparable strength from 1.4 to 6.4 MeV in ^{54}Fe, and a number of other levels in this region with cross sections which are a fair fraction[16] of those for these four states. For ^{54}Fe, it is consequently easier to confuse the contributions from unresolved adjacent peaks with a background which runs through the entire energy region of an inelastic proton group. The study of peak shapes made for the present work reduced this ambiguity to some extent.

B. Asymmetries

The elastic polarization data for ^{28}Si, ^{58}Ni, and ^{60}Ni extend from 10° to about 165°, while the polarization data for ^{54}Fe extend from 15° to 110°. Back-angle polarizations for ^{54}Fe were not obtained since the runs with a tilt of 0° (see above) occurred at the end of an experiment period and were limited by the available cyclotron time. Also, more time (about 8 hours) was spent on the runs with a tilt of 45° in order to obtain a sufficient number of counts around 90° for the weaker inelastic transitions in this nucleus. The elastic polarization data for ^{58}Ni and ^{60}Ni appear to agree well with previous Minnesota data obtained[48] at 40 MeV from 15° to 55°.

The inelastic asymmetry data extend over as much of the angular regions covered by the elastic polarizations as the uncertainties in the inelastic measurements would allow. No meaningful asymmetry data could be obtained for the weaker 3^- state in ^{54}Fe at 4.8 MeV, for which the uncertainties in unfolding the energy spectra amounted to an intolerable probable error in the asymmetry result.

The inelastic asymmetry results are shown in Fig. 4 along with empirical curves drawn through the data to illustrate our judgment of the trends. The curves for the 2^+ states in ^{54}Fe, ^{58}Ni, and ^{60}Ni are all identical and illustrate that,

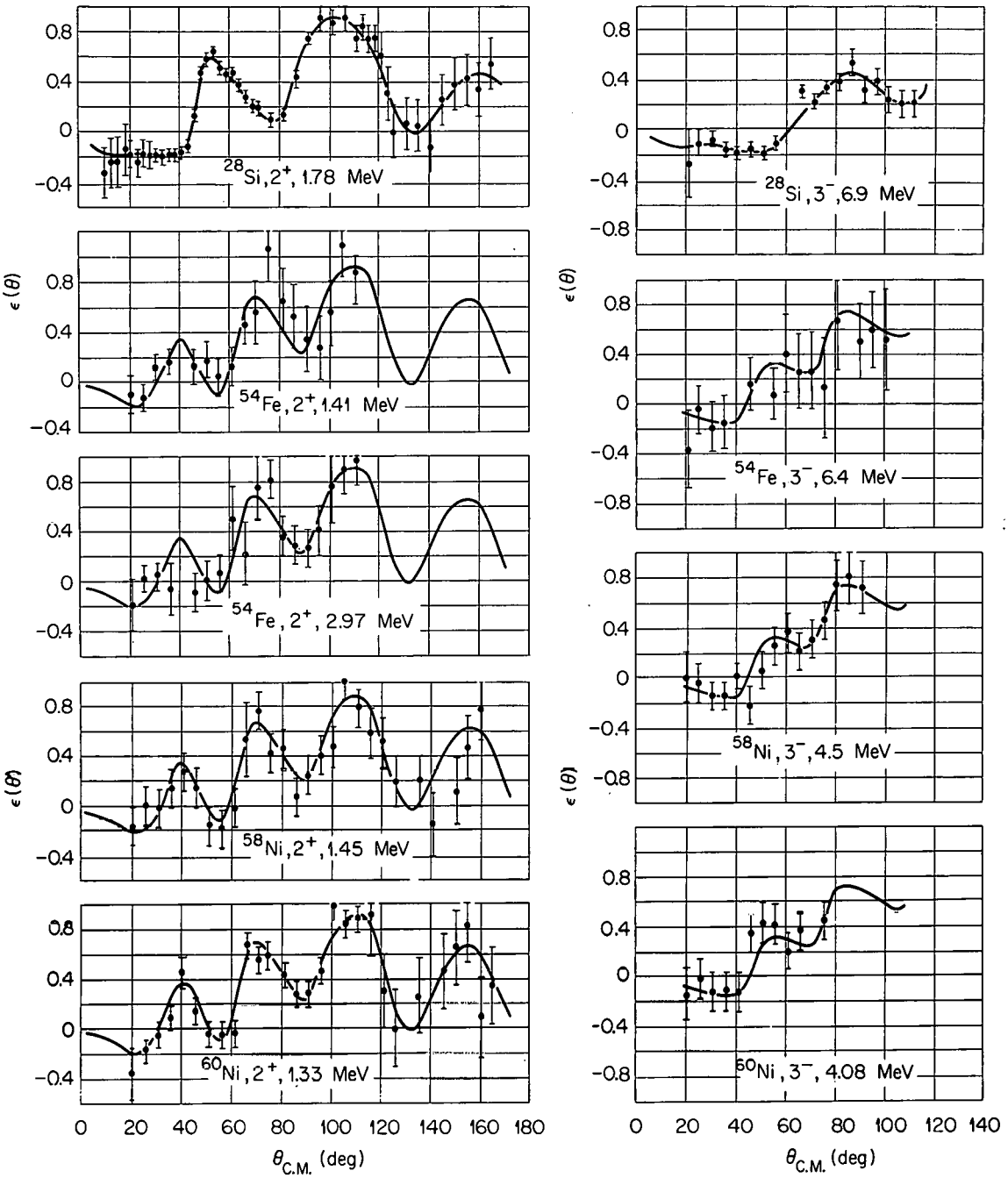

Figure 4. Inelastic asymmetry data. The curves shown are empirical and are identical for transitions in iron and nickel of the same multipolarity. The error bars denote the relative probable errors defined in the text and tabulated in Section VII.

within present uncertainties, these asymmetries are very much alike. The same was done for the curves shown for the 3^- excitations in these nuclei. Agreement of the asymmetry results is particularly clear for the 2^+ states in ^{58}Ni and ^{60}Ni.

Inelastic asymmetries measured[26] with 18.6-MeV protons at Saclay have differed for some of the 2^+ transitions observed in isotopes of Ti, Cr, and Fe. There appeared to be two types, one of which was more similar to 16.5-MeV data[23] for 2^+ excitations in ^{60}Ni and ^{62}Ni. Most notably, a difference was detected between the asymmetries for the 1.41-MeV state in ^{54}Fe and the 2.97-MeV state in the same nucleus. The difference was that the asymmetry for the lower-lying 2^+ state in ^{54}Fe was everywhere larger in algebraic value than that for the second 2^+, by as much as 0.3 at some angles. This amount is considered[26] to be well outside any discrepancy attributable to the different Q values in a collective-model description, which is certainly true of the calculations studied here. A close examination of our data in Fig. 4 in the light of the Saclay results does suggest that the maximum in the asymmetry near 70° for the 1.41-MeV state in ^{54}Fe may be shifted out in angle by about 5°, and may be 0.2 larger, than that for the other three iron and nickel results. But clearly this is not well established by our present data.

The cross sections for the two 2^+ excitations in ^{54}Fe, however, are similar in shape, both at 17.5 MeV[16] and at 40 MeV (from this work and Ref. 42). At 40 MeV the cross sections for both 2^+ states are well described by assuming a one-phonon collective excitation. It would therefore be interesting to see if more accurate asymmetry data for these two excitations in the 40-MeV energy region, where the direct-reaction picture is well established, would reveal some "microscopic difference" not detected in the inelastic cross-section measurements. On the collective model, the agreement in shape and magnitude of the cross sections for the two states in ^{54}Fe would suggest that they involve a considerable mixing of one- and two-phonon vibrations. Attributing a strong two-phonon component to the higher state, however, does not seem consistent with the Saclay asymmetry measurements, since it is the data[26] for that state which agrees more closely with the data[23] for the first excited states in ^{60}Ni and ^{62}Ni. Combining our work and the Saclay results, the asymmetries for the first 2^+ states in ^{48}Ti, ^{56}Fe, ^{58}Ni, ^{60}Ni, and ^{62}Ni appear to agree with that for the second 2^+ in ^{54}Fe, while another kind of result is noticed for the first 2^+ states in ^{50}Ti, ^{52}Cr, and ^{54}Fe. It is curious that the excitations in this second group might all involve a fairly pure $(f_{7/2})^{\pm n}$ proton configuration and a closed neutron shell, while those in the first group are all more complicated.

Our result for the 2^+ excitation in ^{28}Si appears to agree very well with the Birmingham measurements[25] at 30 and 50 MeV, assuming the features of their data extrapolate to 40 MeV. A prominent feature of all the 40-MeV inelastic asymmetries, for both 2^+ and 3^- excitations, consists of the large positive oscillations observed at the larger scattering angles, not unlike the general trend seen in elastic scattering. Also, all of the inelastic asymmetries appear to be negative at the most forward angles where their measurement was possible. These two characteristics of the data will be used frequently in evaluating the success of the collective-model analysis described in the next section.

III. ANALYSIS

Before proceeding to discuss the results of the calculations made for our data, we first review briefly some basic elements of the distorted-waves theory of inelastic scattering. In doing so, we rely extensively on a series of lectures given by G. R. Satchler. After the introduction, we define explicitly the form of the collective-model interaction investigated in our analysis.

1. Theory

A. Distorted-waves Method

One exact expression of the transition amplitude for inelastic scattering from entrance channel $\alpha = A + p$ to exit channel $\beta = A^* + p'$ is given by

$$T_{\alpha\to\beta} = \langle \chi_\beta^{(-)} \psi_\beta \left| V_\beta - U_\beta \right| \Psi_\alpha^{(+)} \rangle \ , \qquad (7)$$

where $\chi_\beta^{(-)}$ is the scattering eigenfunction of a potential U_β between p' and A^* with the asymptotic form $[\exp(i\underset{\sim}{k}_\beta \cdot \underset{\sim}{r}_\beta) + \text{incoming wave}]$, and ψ_β is the wave function of the internal states; here $\psi_\beta = \psi_{A^*}$. $\Psi_\alpha^{(+)}$ is the exact solution of the total Hamiltonian, $H = H_\beta + V_\beta + T_\beta$, with the asymptotic form ψ_α times $[\exp(i\underset{\sim}{k}_\alpha \cdot \underset{\sim}{r}_\alpha) + \text{outgoing wave}]$ in the channel α and purely outgoing waves in all other open channels. V_β is the total interaction in the exit channel,

and H_β describes the internal motion of A^*, $H_\beta \psi_\beta = E_\beta^* \psi_\beta$. The potential U_β is arbitrary. For example, if U_β is the Coulomb potential, χ_β is a Coulomb-distorted wave and $(V_\beta - U_\beta)$ is the purely nuclear interaction; if $U_\beta = 0$ then $\chi_\beta = \exp(i\underset{\sim}{k}_\beta \cdot \underset{\sim}{r}_\beta)$. More significantly, U_β might be chosen so that $(V_\beta - U_\beta)$ could be treated as a perturbation.

The first problem is to find a suitable approximation for the form of the exact solution Ψ, with which calculations can then be carried out to test some choice of effective interaction V and nuclear wave functions ψ. Two preliminary assumptions are made: (i) the possibility of exchange of the projectile with a target nucleon is neglected, and (ii) the effective interaction is taken to be local. In DW calculations, as defined below, exchange might be accounted for to some extent through the use of optical-model wave functions which reproduce the experimentally observed elastic scattering. The effect of non-locality in DW calculations of inelastic scattering has been considered[49] quantitatively and found to reduce the contributions to the transition amplitude for small values of the relative coordinate $\underset{\sim}{r}$ between the projectile and the nucleus. This decreases the magnitude of the predicted cross section by about 20% or, for the same cross section, increases the strength of the effective interaction by about 10%. As is indicated later, our calculations of the shape of the differential cross section and of the asymmetry seem fairly insensitive to contributions from the nuclear interior.

An exact expression for the total wave function is obtained by expanding it in terms of the internal states ψ_j of the target A and the corresponding states, $\xi_j(\underset{\sim}{r}) = \langle \psi_j \mid \Psi \rangle$, of the relative motion between A and p:

$$\Psi_a^{(+)} = \sum_{j=0}^{\infty} \psi_j \, \xi_j(\underset{\sim}{r}) \quad . \tag{8}$$

The entrance channel corresponds to the ground state of the target, say ψ_0, so that only $\xi_0(\underset{\sim}{r})$ has an incoming part. The sum runs over the continuum as well as the bound states of the target. In the "coupled-equations" method, this sum is truncated, commonly at $i = 1$ or 2. For the "distorted-waves" method, only the term $i = 0$ is retained. In either approximation, one expects some modification of the effective interaction and scattering wave functions in order to compensate for the effect of the missing channels.

The total wave function satisfies the Schrödinger equation

$$[H_a + T_a(\underset{\sim}{r}) + V_a(\underset{\sim}{r})] \, \Sigma_j \psi_j \, \xi_j(\underset{\sim}{r}) = E \, \Sigma_j \psi_j \, \xi_j(\underset{\sim}{r}), \tag{9}$$

so that an inner product with ψ_i, using $H_a \psi_j = E_j \psi_j$, yields

$$[(E - E_i) - T_a(\underset{\sim}{r}) - V_{ii}(\underset{\sim}{r})] \, \xi_i(\underset{\sim}{r}) = \sum_{j \neq i} V_{ij}(\underset{\sim}{r}) \, \xi_j(\underset{\sim}{r}) \, , \tag{10}$$

where, calling the target coordinates x,

$$V_{ij}(\underset{\sim}{r}) = \int dx \, \psi_i^{*}(x) \, V_a(\underset{\sim}{r}, x) \, \psi_j(x) \, . \tag{11}$$

The "coupled-equations" approximation is made formally by reducing the sum Σ to a sum Σ' over only a few channels. When this is done, the elements V_{ij} are assumed to become complex-valued potentials U_{ij}, determined by some choice or model for the interaction and nuclear wave functions, whose imaginary part accounts for absorption of flux into the missing channels. One then has a limited set of coupled equations

$$[(E - E_i) - T(\underset{\sim}{r}) - U_{ii}(\underset{\sim}{r})]\, \chi_i(\underset{\sim}{r}) = \Sigma'_{j\neq 1}\, U_{ij}(\underset{\sim}{r})\, \chi_j(\underset{\sim}{r}), \quad (12)$$

with a solution Ψ(C-Eq) composed of scattering wave functions $\chi_j(\underset{\sim}{r})$:

$$\Psi_\alpha^{(+)}(\text{C-Eq}) = \Sigma'_j\, \psi_j\, \chi_j(\underset{\sim}{r}) \ . \quad (13)$$

From Eq. (7), one expression for the corresponding transition amplitude for an excitation from $\alpha = p + \psi_0$ to $\beta = p' + \psi_i$ is

$$T_{0\to i}(\text{C-Eq}) = \langle \psi_i\, \tilde{\chi}_i^{(-)}(\underset{\sim}{k}_i, \underset{\sim}{r}) \,\Big|\, U - U_{ii} \,\Big|\, \Psi_0^{(+)}(\text{C-Eq}) \rangle, \quad (14)$$

where the distorted wave $\tilde{\chi}_i$ is generated by only the potential U_{ii}, i.e. not by the coupled equations (12).

The conventional "distorted-wave Born approximation" consists of reducing Eq. (13) to only one channel:

$$\Psi_\alpha^{(+)}(\text{DWBA}) = \psi_0\, \tilde{\chi}_0^{(+)}(\underset{\sim}{k}_0, \underset{\sim}{r}) \ , \quad (15)$$

where $\tilde{\chi}_0$ is generated by the diagonal potential U_{00},

$(E - E_0 - T - U_{00})\,\tilde{\chi}_0 = 0$. Equation (14) is then replaced by

$$T_{0\to i}\,(\mathrm{DWBA}) = \langle \psi_i\, \tilde{\chi}_i^{(-)}\,(\underset{\sim}{k}_i, \underset{\sim}{r}) \left| U - U_{ii} \right| \psi_0\, \tilde{\chi}_0\,(\underset{\sim}{k}_0, \underset{\sim}{r})\rangle$$

$$= \langle \tilde{\chi}_i^{(-)}\,(\underset{\sim}{k}_i, \underset{\sim}{r}) \left| U_{i0}\,(\underset{\sim}{r}) \right| \tilde{\chi}_0^{(+)}\,(\underset{\sim}{k}_0, \underset{\sim}{r})\rangle, \quad (16)$$

where the second form follows because U_{ii} is diagonal in the states ψ_i. One expects this approximation to Eq. (14) to be good if the coupling between different states is weak. In this form, however, the DWBA gives us no practical simplification, since to obtain the potential U_{00} one still has to solve the coupled equations (12); $\tilde{\chi}_0$ does <u>not</u> give the observed elastic scattering in the entrance channel. Presumably, a better approximation would be to use the exact elastic wave ξ_0 in place of $\tilde{\chi}_0$; and if ξ_0 is in turn approximated by an optical-model solution φ_0, a practical simplification is also obtained. The wave φ_0 is generated by an optical potential U_{OM} which phenomenologically accounts for the observed elastic scattering in the entrance channel. The empirical wave φ_0 should be close to the wave ξ_0 in the exterior region, and the major assumption is that φ_0 is correct in the nuclear interior. With this approximation, one has the so-called "asymmetric distorted-wave approximation":

$$T_{0\to i}\,(\mathrm{ADWA}) = \langle \tilde{\chi}_i^{(-)}\,(\underset{\sim}{k}_i, \underset{\sim}{r}) \left| U_{i0}\,(\underset{\sim}{r}) \right| \varphi_0^{(+)}\,(\underset{\sim}{k}_0, \underset{\sim}{r})\rangle, \quad (17)$$

where, in lieu of solving Eq. (12), some additional assumption must be made about $\tilde{\chi}_i$.

For the "distorted-waves (DW) method" one also uses an empirical wave φ_i in the exit channel.* The DW method is thus based upon the transition amplitude

$$T_{0\to i}\,(\mathrm{DW}) = \int d\underset{\sim}{r}\; \varphi_i^{(-)*}\,(\underset{\sim}{k}_i,\ \underset{\sim}{r})\ \langle \psi_i \left| U \right| \psi_0 \rangle\ \varphi_0^{(+)}\,(\underset{\sim}{k}_0,\ \underset{\sim}{r}), \quad (18)$$

where the distorted waves φ_j are generated by an optical-model potential U_{OM} which is adjusted to reproduce the observed elastic scattering in the channel j,

$$[\nabla^2 + k_j^2 - \tfrac{2\mu}{\hbar^2}\, U_{OM}\,(\underset{\sim}{r})]\ \varphi_j\,(\underset{\sim}{k}_j,\ \underset{\sim}{r}) = 0\ . \quad (19)$$

Whereas in the coupled-equations method the elastic and inelastic scattering are treated simultaneously, by including both channels explicitly, this DW transition amplitude is basically a statement that elastic scattering is by far the dominant process. Specific calculations[8] of ^{56}Fe(p, p') for a collective-model interaction have shown that only for lower energies ($E_p \simeq 10$ MeV) and larger couplings ($\beta_\ell \simeq 0.4$) do the coupled-equations and DW methods give appreciably different angular distributions. We will demonstrate below the equivalence of the methods for our calculations. An important

---

*All phenomenological "DWBA analyses" are made using this "DW method" or, in a few cases, some form of the ADWA. The distinction made here between the DWBA and the DW method is rarely made elsewhere.

exception to this equivalence is the case in which the excited state can be reached not only by a direct excitation (to higher than first order in the coupling interaction) but also through multiple excitation. A two-phonon collective vibration is such a state and must usually be treated with the coupled-equations method.

B. Optical-model Potential

We will now write down the specific forms of the optical-model potential and collective-model interaction used in the present DW analysis. The elastic scattering is described with an 11-parameter optical potential of the standard form:

$$U_{OM}(r) = U_{Coul}(r) - Vf(x) - i(W - 4W_D\, d/dx')\, f(x') + (\hbar/m_\pi c)^2 (V_S + i W_S)\, \vec{\sigma} \cdot \vec{\ell}\, (1/r)\, (d/dr)\, f(x_S), \tag{20}$$

where the Woods-Saxon shape factors are

$$f(x_k) = (e^{x_k} + 1)^{-1}, \quad x_k = (r - r_k A^{1/3})/a_k$$

for each of the "geometry" parameters $r_k = r_0,\ r'_0,\ r_S$; $a_k = a,\ a',\ a_S$. The first term is the Coulomb potential for

a proton in the field of a uniformly charged sphere of radius $R_c = 1.2\ A^{1/3}$ F and charge Ze,

$$U_{Coul}(r) = Ze^2/r \quad \text{if } r > R_c,$$

$$= (Ze^2/2R_c)\,(3 - r^2/R_c^2) \quad \text{if } r \leq R_c. \qquad (21)$$

For proton energies near 40 MeV, the strength V of the real, central (nuclear) term is about 45 MeV for medium-weight targets and decreases with increasing proton energy at the rate $dV/dE_p \simeq -0.22$.[21,32] It also has a symmetry dependence[50,51] on (N - Z)/A, with a coefficient of about 26 MeV.[21] The absorptive, central term is taken to have two components: a "volume" term with a strength W and a Woods-Saxon shape, and a "surface" term with a strength W_D and the derivative of the Woods-Saxon shape. At 40 MeV[20,21] and higher, it becomes important to include some volume component. For lower energy protons (< 30 MeV), purely surface absorption has been used,[51] and at 155 MeV purely volume absorption is adequate.[52] At 40 MeV the strength $(W + W_D)$ is about 8 MeV for medium-A targets and tends to increase slowly with A.[2,20,21] The last term is the spin-orbit potential which is taken to be complex, although there is little evidence yet that the strength W_S of the imaginary part is appreciably different from zero. At 40 MeV, V_S is about 6 MeV.[20,21]

The comprehensive analysis[51] of 9- to 22-MeV proton data by Perey led to the following values for the geometry parameters (with W = 0):

$$r_0 = r_0' = r_S = 1.25 \text{ F}$$

$$a = a_S = 0.65 \text{ F}, \; a' = 0.47 \text{ F} \; .$$

An analysis[2] of 40-MeV elastic cross sections, however, led to the values $r_0 = r_S = 1.18$ F, $a = a' = a_S = 0.7$ F, and (i) $r_0' = 1.04$ F for surface absorption (W = 0), (ii) $r_0' = 1.4$ F for volume absorption ($W_D = 0$). The latest analysis[21] of more extensive elastic cross section and polarization data for eleven targets at 40 MeV gives the following average values for the geometry parameters (using both surface and volume absorption):

$$r_0 = 1.16 \text{ F}, \; a = 0.75 \text{ F}$$

$$r_0' = 1.37 \text{ F}, \; a' = 0.63 \text{ F}$$

$$r_S = 1.06 \text{ F}, \; a_S = 0.74 \text{ F} \; .$$

The optical potentials for the present elastic data are determined by searching simultaneously on both the cross section and polarization measurements for each target. This search is accomplished with a computer routine[7] which attempts

to find parameter values for Eq. (20) which minimize the quantity $(\chi_\sigma^2 + \chi_P^2)$, where

$$\chi_\sigma^2 = \sum_{i=1}^{N_\sigma} \left\{ [\sigma_{EX}(\theta_i) - \sigma_{TH}(\theta_i)]/\Delta\sigma_{EX}(\theta_i) \right\}^2$$

and

$$\chi_P^2 = \sum_{i=1}^{N_P} \left\{ [P_{EX}(\theta_i) - P_{TH}(\theta_i)]/\Delta P_{EX}(\theta_i) \right\}^2 . \quad (22)$$

Here, $\sigma_{EX}(\theta_i)$ and $P_{EX}(\theta_i)$ are the data at angle θ_i, $\sigma_{TH}(\theta_i)$ and $P_{TH}(\theta_i)$ the calculated values, and $\Delta\sigma_{EX}(\theta_i)$ and $\Delta P_{EX}(\theta_i)$ the experimental uncertainties, or weights, assigned to the measurements. Except where noted differently, the relative probable errors defined in Section II-3, and listed in Section VII, were used to weight the elastic data.

C. Collective-model Form Factors

The collective-model (inelastic) interaction appropriate for exciting a 2^ℓ-pole rotation or single-phonon surface oscillation in the target nucleus is obtained by deforming the spherical optical potential (20). This procedure has been described previously[5, 6] in detail. The effective interaction for the DW calculation is taken to be the non-spherical part of the deformed potential which occurs to first order in the multipole deformation parameter β_ℓ. The strength of the resulting nuclear matrix element U_{i0}, and its

dependence on the relative coordinate, are contained in a "form factor" $F(\underset{\sim}{r})$. Historically, only the real, central terms in the optical potential were included, that is, allowed to contribute to the non-spherical interaction. In that case, one has the form factor $F(\underset{\sim}{r}) = f_{Re}(\underset{\sim}{r}) + f_{CE}(\underset{\sim}{r})$, where $f_{Re}(\underset{\sim}{r})$ is the contribution from the nuclear term and $f_{CE}(\underset{\sim}{r})$ is that from the Coulomb term. The latter accounts for the possibility of Coulomb excitation, which has an amplitude adding coherently to the nuclear amplitude. These contributions to the total form factor are given[5] by

$$f_{Re}(\underset{\sim}{r}) = (\beta_\ell R_0 V/a_0) Y_{\ell m} (d/dx) f(x) \qquad (23)$$

and

$$f_{CE}(\underset{\sim}{r}) = 3 \beta_\ell (2\ell + 1)^{-1} Ze^2 R_c^{\ell} Y_{\ell m} r^{-\ell-1} \quad \text{if} \quad r \geq R_c ,$$

$$= 0 \quad \text{if} \; r < R_c \; . \qquad (24)$$

The factors $R_0 = r_0 A^{1/3}$, $a_0 = a$, V, and f(x) are those appearing in Eq. (20) and are determined by fitting the elastic data. Calculations which include only the form factors (23) and (24) are termed "real coupling".

More recently, collective-model calculations have been carried out with "complex coupling", where both real and imaginary parts of the central portion of U_{OM} are deformed. The imaginary part of the non-spherical interaction gives important contributions to the inelastic scattering of ^{3}He and

deuterons and appears necessary to obtain reasonable values of β_ℓ.[19] Complex coupling results in a slight but consistent improvement in predictions of the shapes of the angular distributions for 2^+ and 3^- excitations for 40-MeV protons, but has a small ($\sim 10\%$) effect on β_ℓ.[2] In complete analogy with the real form factor (23), the contribution from the imaginary, central terms in Eq. (20) is

$$f_{Im}(\underline{r}) = i(\beta_\ell R_0' W/a_0') Y_{\ell m} (d/dx') f(x')$$

$$+ i(\beta_\ell R_0' W_D/a') Y_{\ell m} (-4d/dx') (d/dx') f(x'), \qquad (25)$$

where $R_0' = r_0' A^{1/3}$, $a_0' = a'$. The same deformation has been assumed for both real and imaginary parts of the optical potential. In the present work, we also consider a contribution from the spin-orbit term in Eq. (20). The spin-orbit form factor may also be written down by analogy, noting that the factor $(Y_{\ell m} \vec{\sigma} \cdot \vec{\ell})$ is to be made Hermetian:

$$f_{SO}(\underline{r}) = - (\beta_\ell^{SO} R_S/a_S) (V_S + i W_S) (\hbar/m_\pi c)^2$$

$$\cdot (1/2) (Y_{\ell m} \vec{\sigma} \cdot \vec{\ell} + \vec{\sigma} \cdot \vec{\ell} Y_{\ell m}) (1/r) (d/dr) (d/dx_S) f(x_S). \qquad (26)$$

We thus consider the form factor which results from deforming the complete potential (20), i.e. "complex-plus-spin-orbit coupling":

$$F(\underline{r}) = f_{Re}(\underline{r}) + f_{CE}(\underline{r}) + f_{Im}(\underline{r}) + f_{SO}(\underline{r}). \qquad (27)$$

The form taken here for the non-spherical $\vec{\sigma} \cdot \vec{\ell}$ interaction is to be tested phenomenologically by comparison to our data. It is perhaps the simplest such form but is by no means unique. In particular, if one casts the elastic interaction into the familiar Thomas form $\vec{\nabla} V_{SO}(r) \times \vec{v} \cdot \vec{S}$, the spin-orbit term in our spherical optical potential (20) is equivalent to the expression

$$U_{SO}(r) = [2\mu/(m_\pi c)^2] \vec{\nabla} [(V_S + i W_S) f(x_S)] \times \vec{v} \cdot \vec{S} . \quad (28)$$

But if the deformation is introduced into $f(x_S)$ at this point, there are in addition to the term (26) some other contributions to the form factor which arise from the non-radial components of the gradient operator in the above expression. These contributions are very complicated, and at this stage it is considered reasonable to explore the simpler form factor (26). We do, however, allow the strength β_ℓ^{SO} of the spin-orbit interaction to differ from the strength β_ℓ of the central interaction. If $\beta_\ell^{SO} = \beta_\ell$, then in DW approximation the inelastic cross section is simply proportional to β_ℓ^2, and the asymmetry is independent of β_ℓ. For $\beta_\ell^{SO} \neq \beta_\ell$, the shapes of the calculated cross sections and asymmetries depend upon the ratio $(\beta_\ell^{SO}/\beta_\ell)$.

2. Results

To explore the effects of the collective-model form factors in the DW prediction of inelastic asymmetry, a number of calculations was first made for the targets ^{28}Si and ^{60}Ni. The findings were the same for the two nuclei and will be illustrated only for ^{60}Ni.

Different sets of optical-model parameters for ^{60}Ni were available from Ref. 21 and Ref. 2, all of which gave fairly good fits to the elastic cross section out to large angles. But it soon became apparent that, regardless of the contributions [Eqs. (23) to (26)] included in the form factor $F(\underset{\sim}{r})$, a good fit to the inelastic asymmetry data for the 2^+ excitation would not be produced with a potential which did not also give a good fit to the elastic polarization data out to fairly large angles. In other words, we find that the goodness of fit to the inelastic asymmetry seems much more strongly correlated to the quality of fit to the elastic polarization than to the elastic cross section.

This is illustrated in Fig. 5 for the two sets of optical parameters given in Table I. The "best cross section" parameters are the "best fit" results from Ref. 21, which were deduced by analyzing the present elastic data in the manner described above. The "best polarization" parameters were also found by minimizing $(\chi_\sigma^2 + \chi_P^2)$ for the present data, but with greater weights, i.e. smaller errors ΔP_{EX}, assigned

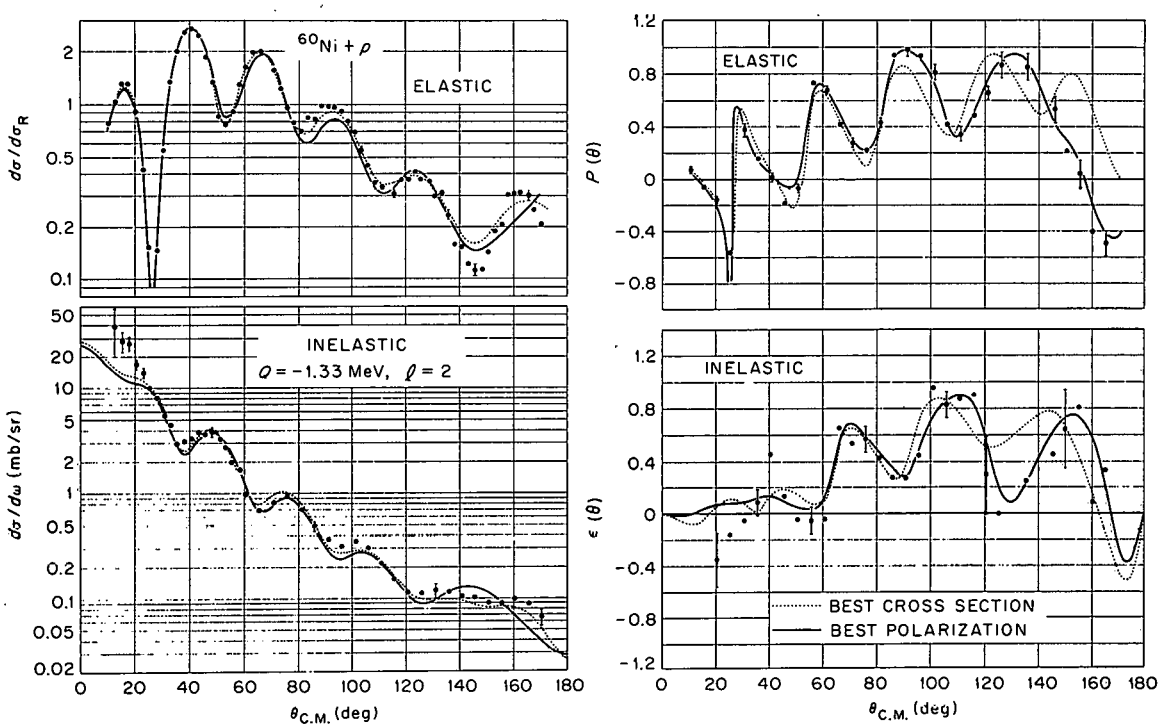

Figure 5. Correlation in fits to elastic and inelastic data. DW calculations are shown for the quadrupole excitation in ^{60}Ni. The two calculations use the two sets of optical-model parameters given in Table I, which produce the elastic fits also shown in the figure.

TABLE I

Optical-model parameters for ^{60}Ni which produce fits to elastic data shown in Fig. 5. The "best cross section" parameters are the "best-fit" values of Ref. 21

Potential	V (MeV)	W (MeV)	W_D (MeV)	V_s (MeV)	W_s (MeV)	r_0 (F)	a (F)	r_0' (F)	a' (F)	r_s (F)	a_s (F)
best cross section	48.3	5.4	1.6	7.0	0	1.12	0.77	1.47	0.60	0.98	0.86
best polarization	52.9	5.5	2.8	4.7	-0.7	1.06	0.87	1.41	0.49	1.04	0.52

to the large-angle polarization data. We return to a discussion of optical-model parameters when the fits to the elastic data from the other targets are described. The calculations of inelastic scattering illustrated in Fig. 5 include all the contributions to the total form factor, with $\beta_2 = 0.22$ and $\beta_2^{SO} = 1.5\,\beta_2$. The effects of the form factors on this calculation and this choice for the strength of the spin-orbit form factor are discussed below.

A total of six potentials (six sets of optical parameters) were tried for ^{60}Ni, each of which fits the elastic cross section and polarization data with a varying degree of success. Different potentials were also investigated for ^{28}Si. In every instance, the calculation of inelastic asymmetry at large angles has failed to reproduce the data over much the same angular region where the fit to the elastic polarization is poor. Because we find the inelastic asymmetry to be quite sensitive to parameter variations, this would seem to add to the credibility of the collective-model-DW treatment. Also, the overall quality of fit to the inelastic cross section has appeared more strongly correlated to the fit to the elastic cross section than to the elastic polarization. These correlations seem consistent with the theory[53] of Austern and Blair in which the elastic and inelastic scattering amplitudes are simply related.

A. Form Factor Studies

The effects of including the different form factors in the calculation of the inelastic scattering from ^{60}Ni are shown in Fig. 6 for the 2^+ excitation and in Fig. 7 for the 3^- excitation. This is illustrated for the "best polarization" potential of Table I, and again we use $\beta_\ell^{SO} = 1.5\,\beta_\ell$ with $\beta_2 = 0.22$ and $\beta_3 = 0.18$. For both the asymmetries and cross sections, the dotted curves are for real coupling only, $F(\underset{\sim}{r}) = f_{Re}(\underset{\sim}{r}) + f_{CE}(\underset{\sim}{r})$. This calculation fails to reproduce the oscillations observed in both the asymmetry and cross section for the 2^+ transition. The curves with short dashes were calculated by adding the spin-orbit form factor to the real form factor, $F(\underset{\sim}{r}) = f_{Re}(\underset{\sim}{r}) + f_{CE}(\underset{\sim}{r}) + f_{SO}(\underset{\sim}{r})$. This increases the absolute value of the asymmetry but still fails to reproduce the oscillations in the 2^+ data. The curves with dots and dashes are for complex coupling, $F(\underset{\sim}{r}) = f_{Re}(\underset{\sim}{r}) + f_{CE}(\underset{\sim}{r}) + f_{Im}(\underset{\sim}{r})$. The oscillations are now larger, but the agreement with the data is not yet good. The asymmetry is not positive enough, and the oscillations in the cross section seem too large. Finally, all the terms are included for the form factor of Eq. (27), which produces the solid curves in these figures.

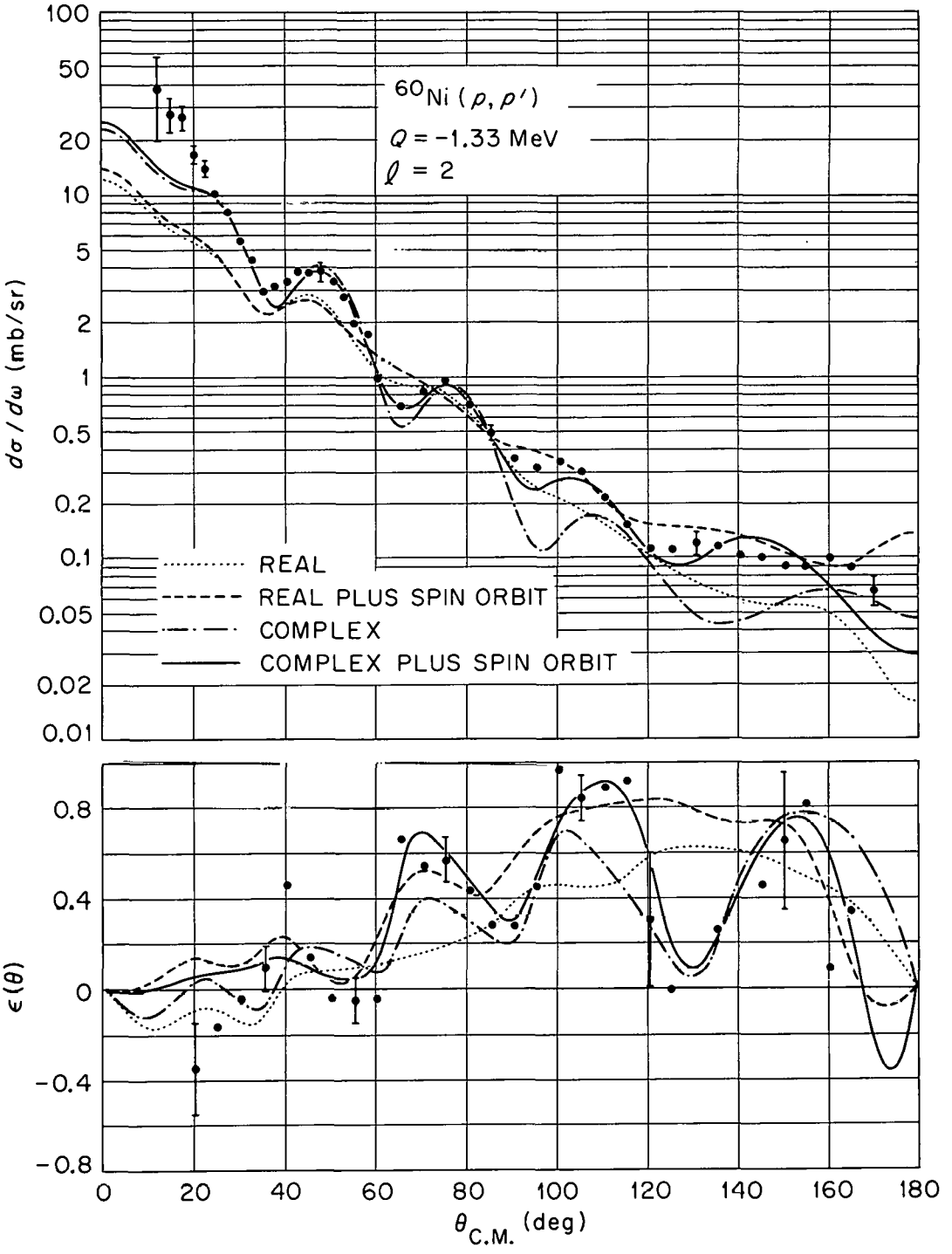

Figure 6. Effects of form factor options for quadrupole excitation. DW calculations are shown for ^{60}Ni in which different contributions to the form factor are included as described in the text.

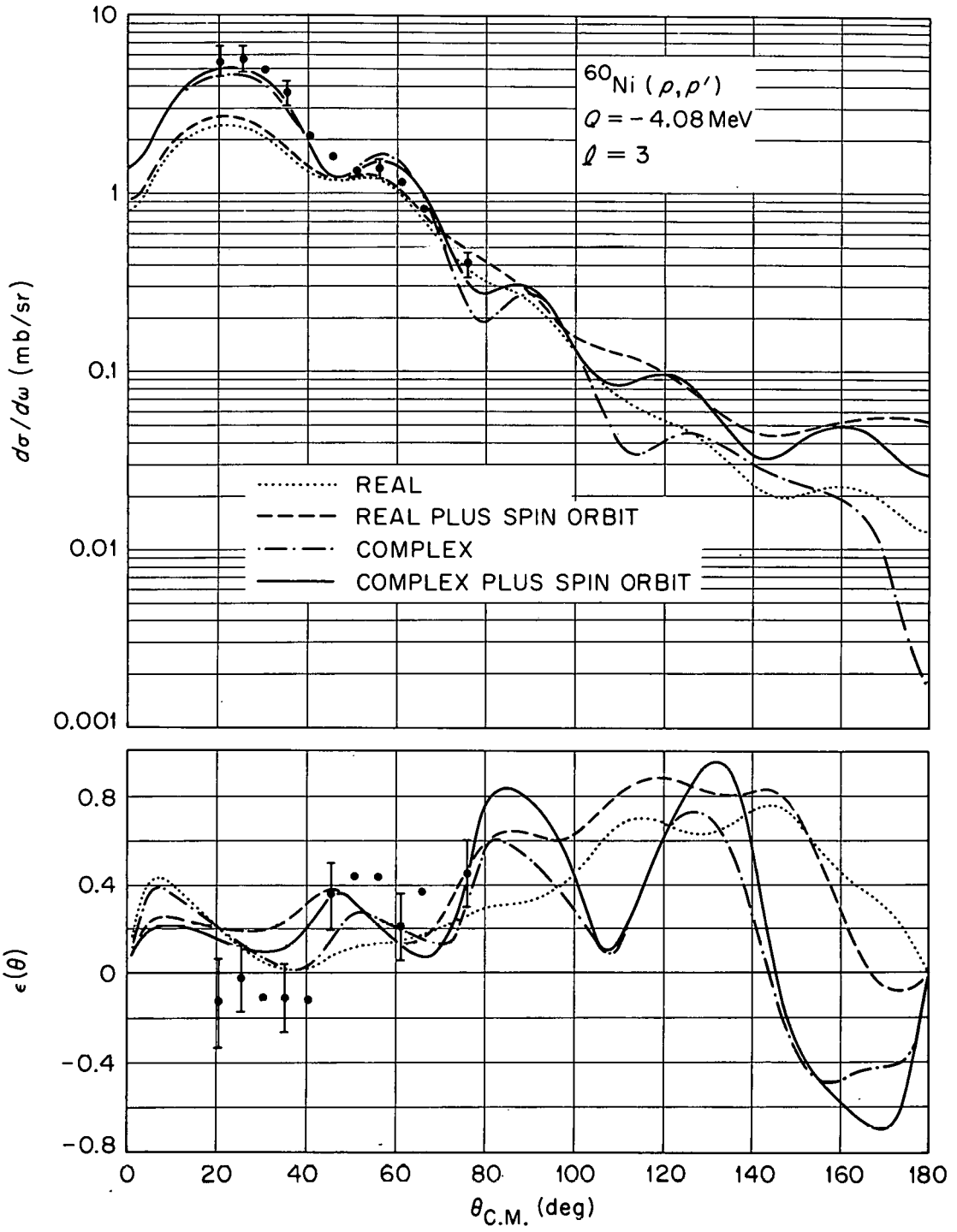

Figure 7. Effects of form factor options for octupole excitation. The calculations of Fig. 6 are repeated for the 3^- state in ^{60}Ni.

For all of the optical potentials tried to date for ^{28}Si and ^{60}Ni, the large positive oscillations observed at large angles in the asymmetry data for the 2^+ excitations appear in the calculations if and only if the imaginary form factor is included. In the calculations of both 2^+ and 3^- asymmetries, the contribution $f_{Im}(r)$ tends to increase the magnitude of the oscillations, while $f_{SO}(r)$ both increases the oscillations and shifts the curve to more positive values. Other collective-model calculations of 2^+ asymmetries have been made for the Saclay Ni data[27] and for the Birmingham ^{12}C and ^{28}Si data[25] using only real coupling. These have also failed to reproduce the large positive oscillations observed in those data at the larger angles. On the other hand the asymmetry data at forward angles, less than about 50° for ^{60}Ni at 40 MeV, are not reproduced by deforming the complete potential in the present treatment. Indeed, our calculations for the 2^+ state in ^{28}Si which do not include the spin-orbit form factor appear slightly better at small angles since they tend to be more negative, like the data. This forward-angle discrepancy will be shown to be quite a general result when the calculations are presented for the rest of our inelastic data. The cross section calculation for the 2^+ state in ^{60}Ni also appears to be a little low at angles smaller than 20°, although this is not generally true for the other 2^+ excitations we measure.

The relative strength ($\beta_\ell^{SO}/\beta_\ell$) of the spin-orbit form factor has been taken to be 1.5 for these and the rest of our calculations, although this choice is somewhat arbitrary. The effect of varying the strength of the spin-orbit form factor is illustrated in Fig. 8 for the same 2^+ calculation shown thus far, using the "best polarization" potential of Table I and the complete form factor (27). A slight but consistent preference for a value of β_ℓ^{SO} about one to two times that of β_ℓ has been found for both the 2^+ cross sections and asymmetries at larger angles. As is indicated in Eq. (26), both real and imaginary parts of the spin-orbit potential are deformed with the same strength β_ℓ^{SO}. However, since all of our results for the optical potential have $\left| W_S \right| << V_S$, calculations which include the imaginary part in the spin-orbit form factor differ very little from those which do not.

Some investigation was made of the effect on the inelastic asymmetry calculation of varying the spin-orbit geometry parameters from their "best polarization" values of Table I. The 2^+ calculation for ^{60}Ni was made for values of these parameters in the range $1.0\ F \leq r_S \leq 1.2\ F$ and $0.5\ F \leq a_S \leq 0.7\ F$. The rest of the optical parameters were not re-adjusted; the fit to the elastic data was not preserved. These changes were made separately (i) in only the form factor $f_{SO}(\underset{\sim}{r})$; (ii) in only the elastic distortion, i. e. in the optical potential used to generate the distorted waves; and

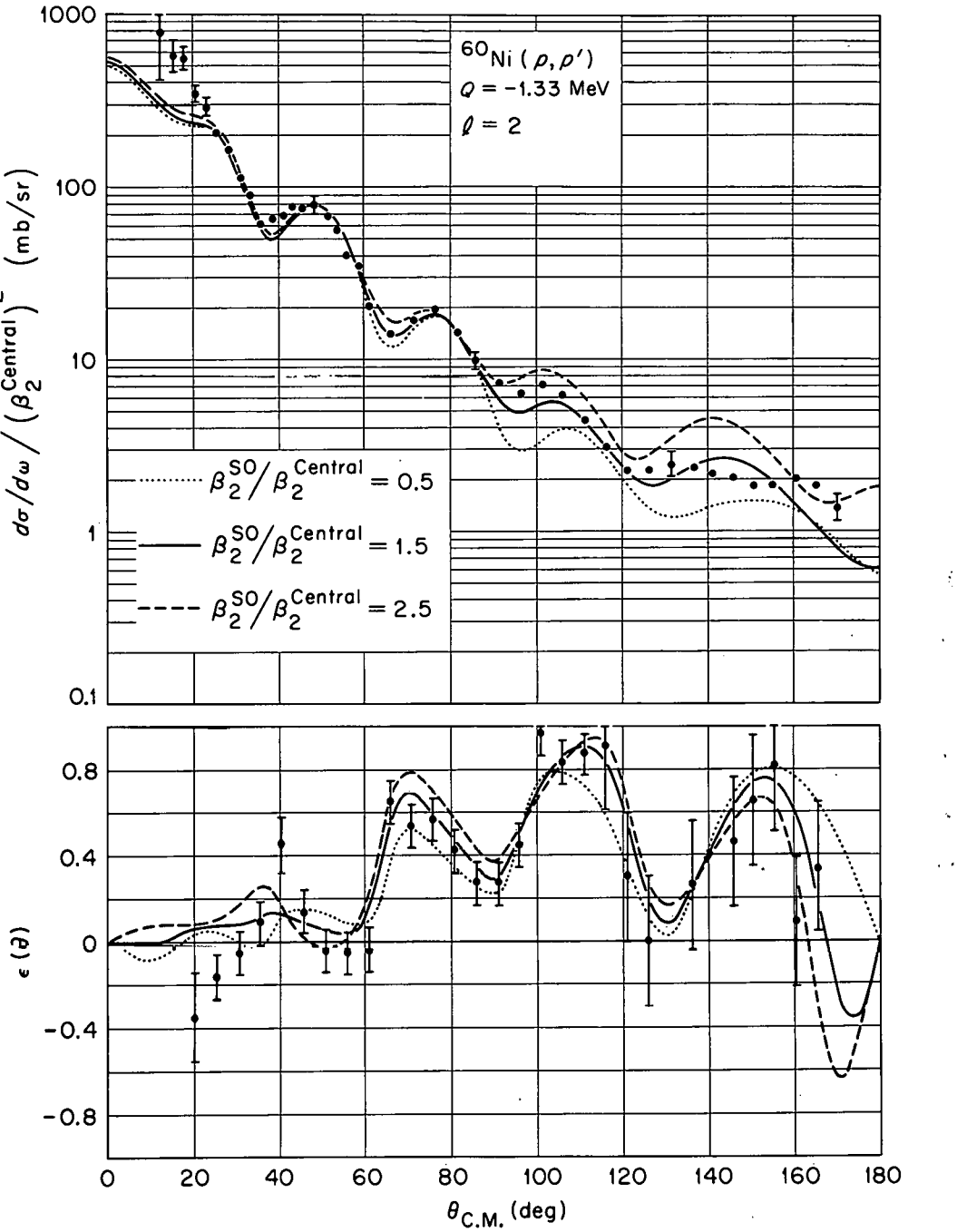

Figure 8. Relative strength of spin-orbit form factor. DW calculations are shown for the quadrupole excitation in ^{60}Ni which use different ratios of the deformation parameters for the spin-orbit and central parts of the optical potential. The cross-section data are plotted for $\beta_2^{Central} = 0.22$.

(iii) in both the form factor and the distortion. For each change the four types of form factor of Fig. 6 were used. In short, no difference in the general features of the asymmetry curves in Fig. 6 was produced. Their relative degree of positiveness and amount of oscillation remained unchanged; in no case was the predicted asymmetry negative at the most forward angles.

In an attempt to judge the importance of the imaginary form factor $f_{Im}(r)$ in our treatment, we have tried to reproduce the observed asymmetry with calculations in which this form factor is left out and the real form factor $f_{Re}(r)$ is varied. In this way, one might hope to bracket the outcome of a "microscopic"[14] DW calculation of the asymmetry made with a real-valued form factor. The distortion was still determined by the fit to the elastic scattering, but the real form factor was no longer given by its collective-model prescription. In doing this, we used the shape of the collective-model form factor (23) but varied its width and radial position by changing its parameters R_0 and a_0 from their optical-model values $r_0 A^{1/3}$ and a, i.e. from the values used for the distorted waves. The calculations were carried out for the 2^+ state in ^{60}Ni with the distortion given by the "best polarization" potential of Table I. At each of the values R_0 = 0.7, 1.0, and 1.3 times the collective-model radius ($r_0 A^{1/3}$), calculations were made for a_0 = 0.5, 0.8, 1.0, 1.2,

and 1.5 times the collective-model diffusivity a. For each of these, the calculation was made with and without including the spin-orbit contribution $f_{SO}(\underset{\sim}{r})$. The Coulomb-excitation contribution $f_{CE}(\underset{\sim}{r})$ was included throughout.

The result of this study was that for any of the radii R_0, and with or without a spin-orbit contribution $f_{SO}(\underset{\sim}{r})$, large oscillations in the inelastic asymmetry comparable with those observed at larger angles were produced only with the most sharply-peaked form factor having the diffusivity parameter a_0 of 0.5 times the collective model value a = 0.87. But with this diffusivity, the asymmetry data were still not reproduced. For $R_0 = 0.7\ r_0\ A^{1/3}$ and $a_0 = 0.5$ a, the asymmetry calculation was negative at larger angles, with or without a contribution $f_{SO}(\underset{\sim}{r})$. For $R_0 = 1.0\ r_0\ A^{1/3}$ and $a_0 = 0.5$ a, the asymmetry calculations became positive, but the oscillations were almost exactly out of phase with the data. For $R_0 = 1.3\ r_0\ A^{1/3}$ and $a_0 = 0.5$ a, the angular interval between oscillations was much less than that observed. The inelastic cross section was poorly reproduced in every case, although subjectively the cross section calculations agreed far better with the data than did the asymmetry calculations. Except for the collective-model values of R_0 and a_0, the main disagreement with the shape of the cross-section data was a difference in phase of up to ± 10° in the forward hemisphere. We conclude that, for the set of real-valued form factors

examined, the contribution $f_{Im}(\underset{\sim}{r})$ is essential in reproducing the oscillations observed at larger angles in the inelastic asymmetry for this 2^+ excitation.

To change the prediction of the inelastic asymmetry at forward angles, one might expect to have to modify the "tail" of the form factor $F(\underset{\sim}{r})$ for large values of r. The largest contribution there to our present form factor is the Coulomb excitation term $f_{CE}(\underset{\sim}{r})$. However, it is shown in Fig. 9 that the calculations made with this term left out altogether are nearly identical to those which include it. This is illustrated for the same ^{60}Ni calculation used previously; the effect of Coulomb excitation is even less for a 3^- excitation. We have also examined the effect of making the Coulomb form factor complex valued. In the same spirit as for the nuclear interaction, an imaginary Coulomb form factor could arise from populating higher excited states of the target by Coulomb excitation. However, one should then have an imaginary Coulomb term in the optical potential which, together with β_ℓ, would determine the strength of its corresponding form factor for the DW calculation. In lieu of starting with a new form of the optical potential, a reasonable guess for the maximum strength of an imaginary Coulomb form factor should be something like $(W + W_D)/V \simeq 0.2$ times that of the real Coulomb form factor. In Fig. 9 a calculation is shown in which an absorptive Coulomb form factor is added with the

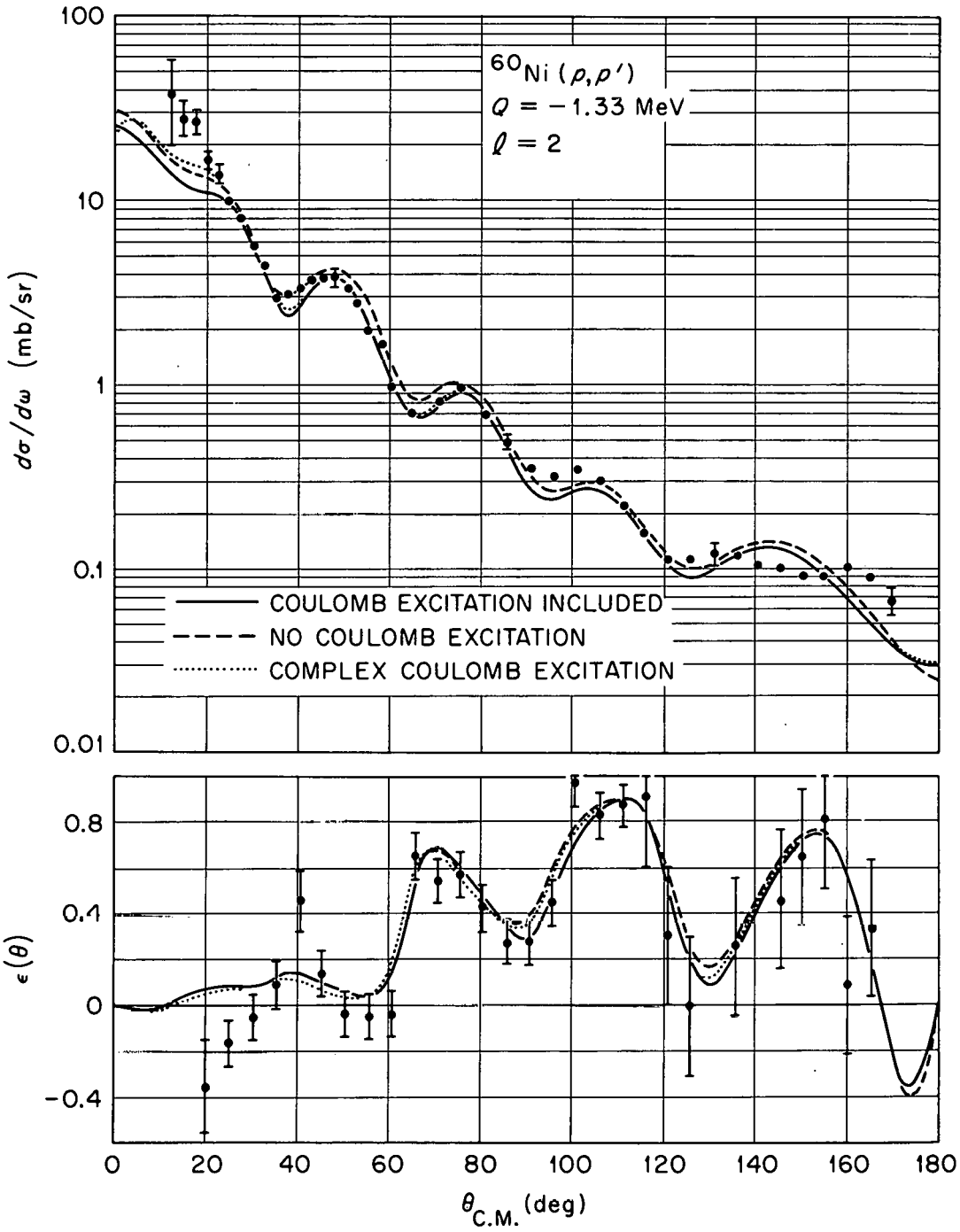

Figure 9. Effect of Coulomb excitation. The solid curves are DW calculations which include the Coulomb excitation contribution, and the dashed curves do not. The dotted curve is the result for a complex-valued Coulomb interaction, as described in the text.

full strength of the real part, i.e. a "complex Coulomb excitation" interaction is included in which $f_{CE}(r)$ is replaced by $f_{CE}(r) - if_{CE}(r)$. This, however, also has a negligible effect. In the rest of our calculations, we include only the usual term $f_{CE}(r)$.

We note that our calculations of inelastic asymmetry are very nearly identical to calculations of the inelastic polarization made in the same way. While the difference $(P - \epsilon)$ varies considerably with the form-factor options of Fig. 6, and increases with the magnitude of Q, it was in no case very large. The present collective-model interaction, including the spin-orbit contribution, gives rise to an angular-momentum transfer to the nucleus of only $j = \ell$. There is, however, a probability for projectile spin-flip in the "overall" collision, with or without the contribution $f_{SO}(r)$, due to the $\vec{\sigma} \cdot \vec{\ell}$ coupling in the elastic distortion. This probability is related to the difference $(P - \epsilon)$ and to the population of the magnetic substates of j. We would therefore expect the effect of $f_{SO}(r)$ to also show up in collective-model calculations of p'-γ angular correlations, and comparison to such data would be another test of the present spin-orbit interaction. In the calculations for the 2^+ excitations in iron and nickel, we find $0 \lesssim (P - \epsilon) \lesssim 0.005$ at forward angles and $0 \lesssim (P - \epsilon) \lesssim 0.01$ at back angles. For the 3^- states, with $Q \simeq 5$ MeV, the difference is larger and

usually of the opposite sign: $0 \lesssim (\epsilon - P) \lesssim 0.05$ at forward angles and $0 \lesssim (\epsilon - P) \lesssim 0.1$ at back angles.

B. ADWA and Coupled Equations

The DW calculation for ^{60}Ni was compared to a form of the ADWA, and the validity of the DW method was explored by comparison to a coupled-equations calculation. In our DW calculations here, we do not modify the optical parameters used for the exit-channel distortion from those used for the entrance channel, i.e. from those which fit the elastic scattering data at the entrance-channel energy. This approximation is substantiated by calculations in which the DW exit-channel parameters V, W, and W_D were corrected for the difference in energy according to the results of our previous study[21,32] of their energy dependence near 40 MeV: $dV/dE_p \simeq -0.22$, $dW/dE_p \simeq 0.2$, $dW_D/dE_p \simeq -0.15$. This produced no appreciable difference from the "uncorrected" calculations. To simulate the ADWA of Eq. (17), we have followed a procedure suggested by Bassel[54] and reduced W and W_D by 20 percent from their entrance-channel values for both the exit-channel distortion and the form factor $f_{Im}(r)$. The major effect of doing this in a calculation for the 2^+ transition in ^{60}Ni was to make the minima in the asymmetry near 90° and 130° less deep (more positive). This was true for calculations using either complex coupling

or the complete form factor (27). For the interactions assumed, then, we find this form of the ADWA to give a poorer prediction than the DW method.

A two-channel, coupled-equations calculation was made including the ground state and the 2^+ state of ^{60}Ni. To make use of the options readily available in the current coupled-equations code[55] at ORNL, a complex-coupling calculation of the inelastic polarization (not the asymmetry) was made which did not include the Coulomb excitation amplitude. Also, a form of the optical potential was used in which the values of the spin-orbit geometry parameters r_S and a_S are taken equal to the values of r_0 and a for the real central term, and the spin-orbit term is taken to be real, $W_S = 0$. The solid curves in Fig. 10 are the elastic and inelastic predictions using a coupling strength of $\beta_2 = 0.22$ and the "best polarization" parameters of Table I, with the changes $r_S = 1.06$ F, $a_S = 0.87$ F, and $W_S = 0$. No reduction in W or W_D was made for these predictions.

To compare these calculations to our DW treatment, we must first obtain new optical-model parameters which, in a one-channel calculation, give the same elastic scattering as the coupled-equations calculation. The dashed curves in Fig. 10 for the elastic cross section and polarization were produced by searching on the elastic coupled-equations predictions out to 120° with the optical-model code Hunter.[7]

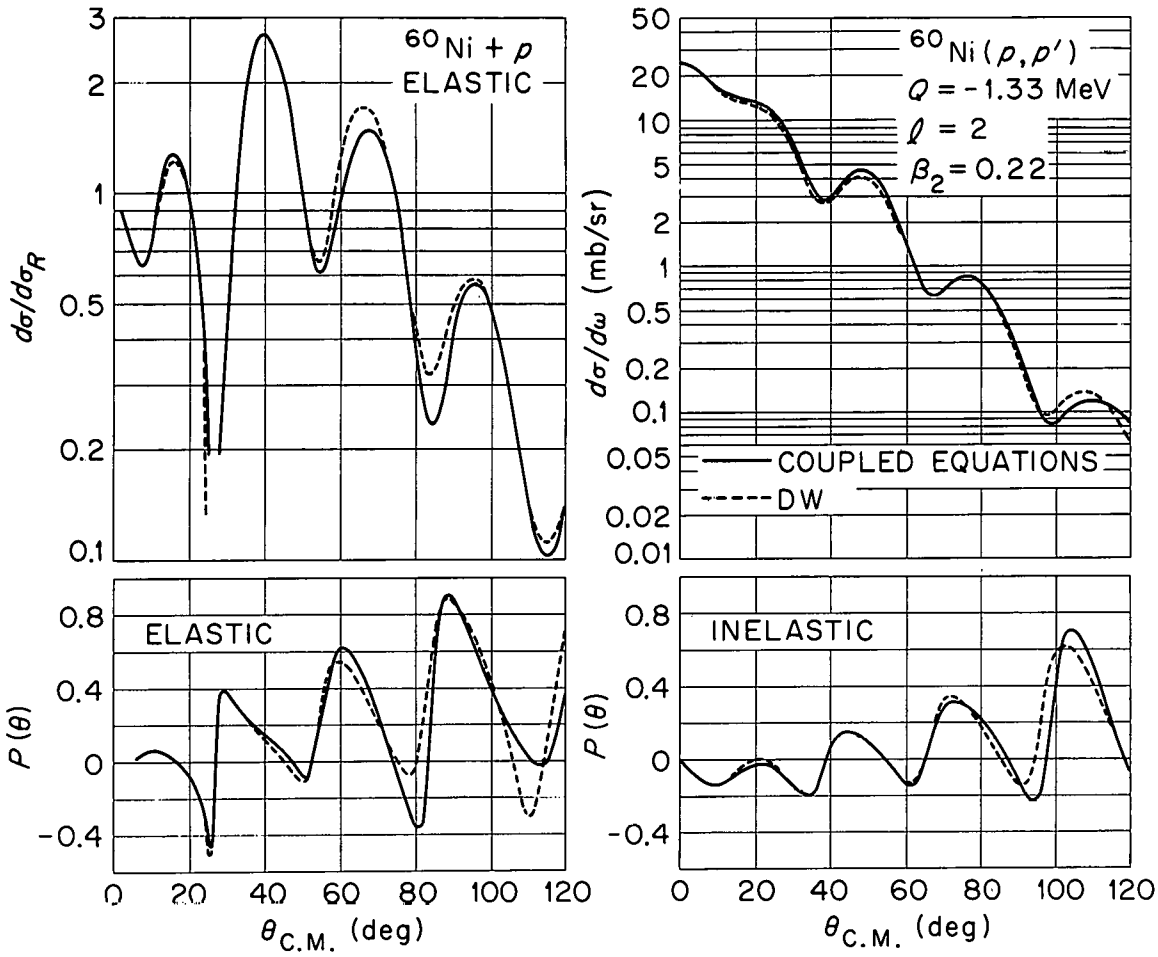

Figure 10. Comparison to coupled-equations calculation. The solid curves are coupled-equations predictions of elastic and inelastic scattering using the parameters given in the text. The dashed curves for elastic scattering are optical-model (one-channel) fits to the coupled-equations results produced by varying only the parameters W and W_D. The dashed curves for inelastic scattering are the DW calculations using this optical potential.

Only the parameters W and W_D were varied from the values used in the coupled-equations calculation; the fits could presumably be improved if all the parameters were varied. The new values found were W = 6.55 MeV and W_D = 2.25 MeV. Thus, W increased by 20 percent from the coupled-equations value, but W_D decreased 20 percent; the sum $(W + W_D)$ increased only 6.4 percent. The dashed curves for the inelastic cross section and polarization are DW results using the optical parameters with these "corrected" absorptive strengths. Their agreement with the coupled-equations results for the inelastic scattering is seen to be at least as good as the agreement produced for the elastic scattering. One-channel calculations were also made using the same (uncorrected) parameters used in the coupled-equations method, and the results for the elastic and inelastic scattering were nearly identical to those using the modified values of W and W_D.

These results are also pertinent to a simplification which is commonly used in coupled-equations calculations. In practical coupled-equations analyses of inelastic cross sections for lower-energy proton scattering, optical-model parameters have sometimes been used which, to save time, are derived by fitting the elastic data with only a one-channel calculation.[10] The coupled-equations calculation is then carried out using these parameters but with the absorptive strength reduced by

some 20% to compensate for the loss of flux from the elastic channel to the inelastic channels now included explicitly. This correction is made in both the diagonal and off-diagonal potentials U_{ij}, and the coupling strengths β_ℓ are then adjusted to produce agreement with the inelastic data. We have also compared coupled-equations calculations for the 0^+ (ground)-2^+ states in ^{60}Ni to the one-channel results, for which the strengths W and W_D were 20% lower in the coupled-equations calculation. This was done for different values of W and W_D used in the one-channel calculation, using a 20% reduction for the coupled-equations calculation in each case. While this procedure produces an agreement in the shape of the elastic and inelastic cross sections which is comparable to that shown in Fig. 10, the agreement for the elastic and inelastic polarizations is noticeably worse. It therefore appears that the correction for absorption which should be made at 40 MeV for $\beta_2 \simeq 0.2$ is much less than 20%, presumably because more exit channels are open at 40 MeV and the 2^+ excitation is responsible for a smaller fraction of the total absorption. This is also consistent with our result for the ADWA, where reducing W and W_D by 20% gave a poorer prediction.

C. Optical-model Parameters

After making these preliminary studies for ^{28}Si and ^{60}Ni, calculations were then carried out for all of our data in a systematic fashion. The first task was to find optical-model parameters for the four targets which would give good fits to the elastic polarization data while sacrificing the fits to the elastic cross-section data as little as possible. Our polarization data for ^{28}Si, ^{58}Ni, and ^{60}Ni are more extensive, and calculations were first made for these targets with errors ΔP_{EX} assigned at large angles which were smaller than the experimental uncertainties. Using the results of these calculations as starting values for the parameters, with the ^{54}Fe potential taken equal to that found for ^{58}Ni, searches were then made for the four targets using exclusively the experimental uncertainties to weight $(\chi_\sigma^2 + \chi_P^2)$. However, the "final" parameter values were taken at that point when the search routine would start to sacrifice the fit to the general trend of the back-angle polarization data in order to achieve a slight improvement in $(\chi_\sigma^2 + \chi_P^2)$, as happened for all three targets ^{28}Si, ^{58}Ni, and ^{60}Ni. In this way we have emphasized the elastic polarization data to some extent, and the optical-model parameters thus found display a consistent difference from those deduced in a previous analysis[21] of these same data, one which relied more strongly on the $(\chi_\sigma^2 + \chi_P^2)$ criterion using the experimental uncertainties for ΔP_{EX}.

The resultant fits to the elastic data are shown in Fig. 11; and the optical parameters, predicted reaction cross sections σ_R, and values of χ^2/N are listed in Table II. The χ^2 values correspond to the experimental uncertainties listed in Section VII. The results were not entirely successful for ^{28}Si and ^{54}Fe, while fairly good fits to the data were obtained for ^{58}Ni and ^{60}Ni. Subjectively, the present fits to the cross-section data appear very similar in quality to those of Ref. 21. For ^{54}Fe, the previous cross-section fit is slightly better near 90°; for ^{60}Ni the present fit is slightly better near 90°; and for ^{28}Si and ^{58}Ni the cross-section fits are very much alike. The fits to the polarization data for ^{54}Fe are also quite similar, but the present potentials somewhat improve the fits to the back-angle polarizations for ^{28}Si, ^{58}Ni, and ^{60}Ni while producing a similar fit at forward angles. For ^{28}Si, the previous calculation of the polarization is about 20° out of phase with the data near 110°, while the present calculation is a little closer. For ^{58}Ni and ^{60}Ni, the previous calculation (see Fig. 5) gave an extra oscillation near 140° which is not observed in the data, and which is eliminated in the present fits.

For comparison to Table II, the previous "best-fit" parameters[21] for these data are listed in Table III. Although the same weights $\Delta\sigma_{EX}$ and ΔP_{EX} were used, it can be noticed that the value of χ^2 does not always reflect a subjective

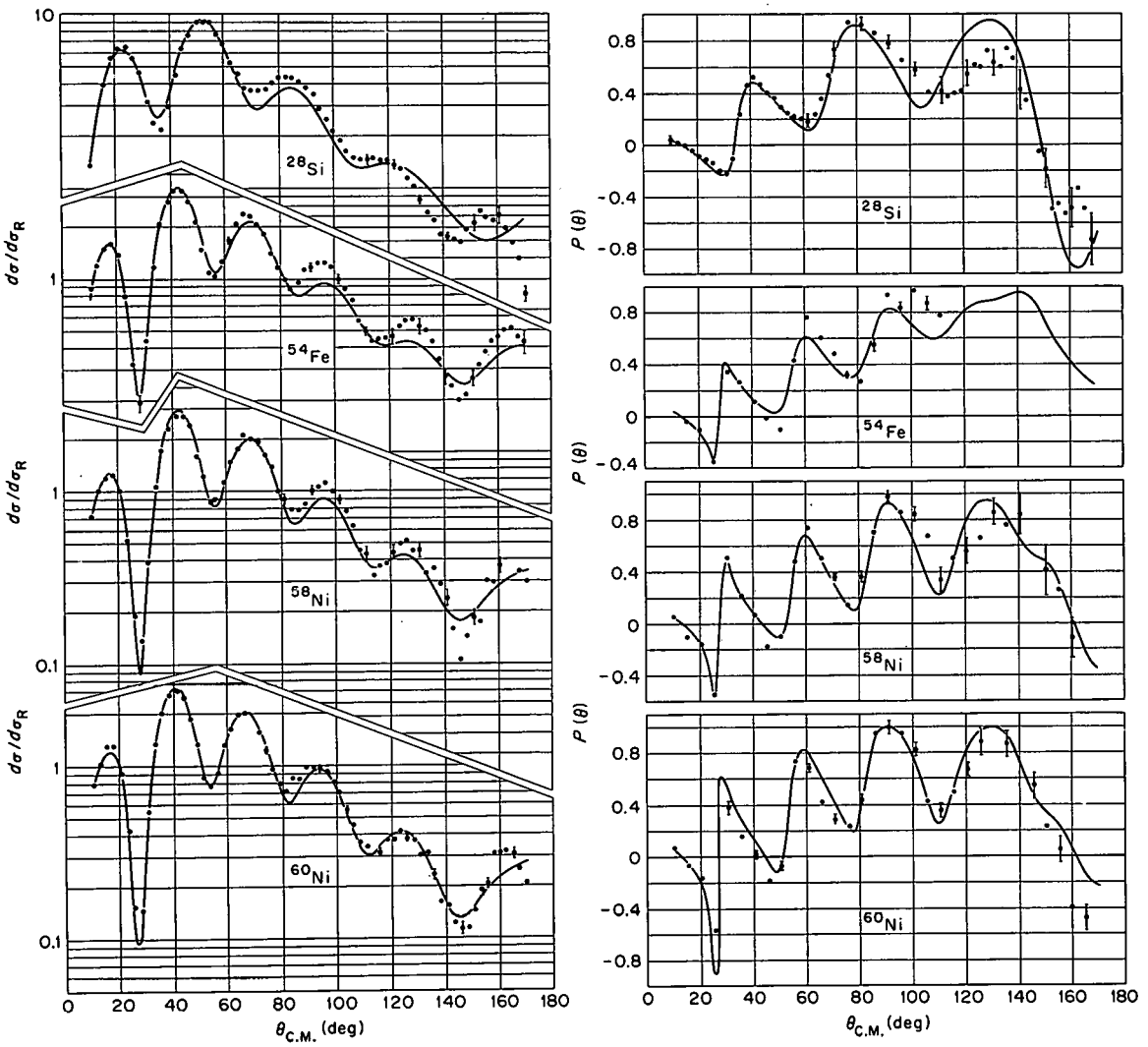

Figure 11. Elastic cross-section and polarization data and their optical-model fits using parameters of Table II.

TABLE II

Present 40-MeV optical-model parameters which produce fits to elastic data shown in Fig. 11.

Nucleus	V (MeV)	W (MeV)	W_D (MeV)	V_s (MeV)	W_s (MeV)	r_0 (F)	a (F)	r_0' (F)	a' (F)	r_s (F)	a_s (F)	$\frac{\chi^2_\sigma}{N_\sigma}$	$\frac{\chi^2_P}{N_P}$	σ_R (mb)
^{28}Si	44.61	1.39	4.41	5.84	-0.36	1.134	0.733	1.409	0.537	1.012	0.632	30.1	13.5	645
^{54}Fe	47.61	5.06	0.12	4.41	-0.61	1.104	0.800	1.587	0.583	1.045	0.659	7.9	20.8	998
^{58}Ni	51.11	5.71	0.74	5.19	-0.24	1.080	0.798	1.531	0.430	1.043	0.614	6.3	21.1	1019
^{60}Ni	51.59	4.70	3.55	7.03	-0.77	1.081	0.815	1.410	0.525	0.975	0.789	8.0	8.1	1104

TABLE III

Previous 40-MeV "best-fit" optical-model parameters from Ref. 21

Nucleus	V (MeV)	W (MeV)	W_D (MeV)	V_s (MeV)	W_s [a] (MeV)	r_0 (F)	a (F)	r_0' (F)	a' (F)	r_s (F)	a_s (F)	$\frac{\chi^2_\sigma}{N_\sigma}$	$\frac{\chi^2_P}{N_P}$	σ_R (mb)
^{28}Si	44.11	3.19	1.98	6.47	0	1.178	0.709	1.560	0.486	1.089	0.741	23.7	11.9	638
^{54}Fe	41.43	6.40	2.47	5.30	0	1.208	0.761	1.279	0.609	1.188	0.679	3.8	23.3	990
^{58}Ni	49.49	6.50	0.52	5.53	0	1.109	0.782	1.477	0.495	1.071	0.641	5.4	25.0	1023
^{60}Ni	48.28	5.41	1.58	7.03	0	1.120	0.769	1.470	0.597	0.979	0.856	6.0	17.8	1126

[a] W_s was held fixed at zero for these searches.

judgment of the fit. For example, the previous value of χ_σ^2 for ^{60}Ni is less than the present value, and so is the value of χ_P^2 for ^{28}Si. The present sum ($\chi_\sigma^2 + \chi_P^2$) is 20% worse for ^{28}Si, 5% worse for ^{54}Fe, 10% better for ^{58}Ni, and 35% better for ^{60}Ni. It can also be seen that unless a measurement of the total reaction cross section were accurate to about one percent or better, the potentials of Tables II and III could not be distinguished in that way. No measurements of reaction cross sections have yet been made at 40-MeV energy, and one can only say that the predicted values appear consistent with measurements made near this energy (see Ref. 2 for a summary of these). We rarely find[2,20,21] potentials at this energy which give reaction cross sections differing by more than about 5 percent.

The values of the spin-orbit geometry parameters r_S and a_S vary considerably from target to target and also between the previous and present results. In the process of obtaining the present fits, however, it was observed that a rather wide range of these parameter values produce reasonable fits. For ^{60}Ni, changing r_S from 1.05 F to 1.00 F and a_S from 0.5 F to 0.7 F, together with very minor changes in the rest of the parameters, gave somewhat better fits to the cross section with only a slight sacrifice of the polarization fit. In going from r_S = 1.00 F to r_S = 0.975 F,

and from $a_S = 0.7$ F to $a_S = 0.8$ F, the last "bump" in the cross section at 160° begins to come into better agreement at the expense of the polarization at the same angle. For values of a_S much greater than 0.80 F, the polarization fit becomes much worse while the cross section fit is only slightly improved. This tendency of the polarization data to favor smaller values of a_S has also been found in an analysis[56] of 30-MeV data. The present results have smaller values of both r_S and a_S than the previous results for these data. Both results give values of r_S which are consistently smaller than those for the real radius r_0. The present values have an average of $(r_0 - r_S)$ equal to 0.08 F, as compared with the previous[21] average for eleven targets of 0.10 F, and the previous average for the four targets here of 0.07 F.

The geometry parameters r_0' and a' in Table II also vary considerably from target to target, but in a way consistent with previous findings for the imaginary potential. It has been found[2] that the cross sections for 40-MeV protons are fit equivalently by imaginary potentials which may differ in the nuclear interior but which are similar in their "tails", say for $r \gtrsim r_0 A^{1/3}$. To produce a tail with a volume potential ($W >> W_D$) which is similar to that for a surface form ($W << W_D$), then the volume potential must have a radius parameter r_0' which is larger than that for the surface potential.

This is consistent with the values of Table II in that ^{54}Fe and ^{58}Ni have $r_0' \simeq 1.55$ F and $W >> W_D$, while ^{28}Si and ^{60}Ni have $r_0' \simeq 1.41$ F and more comparable values of W and W_D.

The greatest difference between the previous[21] and present 40-MeV potentials is believed to be in the geometry parameters found for the real, central well. For each of the three targets with large-angle polarization data, a significant improvement in the fits to those data always occurred at that point in the automatic searching procedure when the radius parameter r_0 became smaller and the diffusivity a became larger. Tables II and III reflect a consistent decrease of 0.03 to 0.04 F in the present value of r_0 for these three targets and an increase of 0.02 to 0.04 F in the value of a. While this is only a change of some four percent in the parameter values, the preference of the polarization data for the new values seems quite strong. However, better large-angle polarization data and more extensive analysis will be necessary at 40 MeV to establish confidently the values of these parameters to such an accuracy. We note also that the radius parameter r_0 seems to be smaller for the Ni isotopes than for the other targets, both in the present work and in the previous analysis of the data for eleven targets.

D. Predictions of Inelastic Scattering

Using the potentials of Table II, we have carried out DW calculations for all of the inelastic transitions. For these, we used consistently $(\beta_\ell^{SO}/\beta_\ell) = 1.5$ and the real-valued Coulomb interaction $f_{CE}(\underset{\sim}{r})$. Each of the form factor options, real and complex coupling, with and without $f_{SO}(\underset{\sim}{r})$, were used again for every excitation, with the same results as those illustrated in Fig. 6 and Fig. 7. The new results are not repetitious since different optical parameters are involved. In particular, the potential for ^{58}Ni has almost pure volume absorption ($W = 7.7\ W_D$), while that for ^{60}Ni is more evenly mixed ($W = 1.3\ W_D$). Yet the DW calculations, including those with a contribution $f_{Im}(\underset{\sim}{r})$ to the total form factor, are almost identical. It has been verified by calculation, however, that the inelastic asymmetry is fairly sensitive to <u>arbitrary</u> changes in the strength or shape parameters of the imaginary form factor $f_{Im}(\underset{\sim}{r})$. By plotting the radial dependence of each of the form factors derived from the optical parameters of Table II, it has been observed that the form factors for ^{58}Ni agree very closely to those for ^{60}Ni in their "tails", $r \gtrsim 6$ F. However, the form factors $f_{Im}(\underset{\sim}{r})$ and $f_{SO}(\underset{\sim}{r})$, which contain the second derivative of the Woods-Saxon potential, are quite different for the two targets in the nuclear interior, say $r \lesssim 5$ F. The same is true for the radial shapes of the imaginary and

spin-orbit terms in the optical potential, in that the terms for ^{58}Ni and ^{60}Ni agree well only in their tails. Although the imaginary term in the optical potential for 40-MeV protons is consistent with a mean free path for a reaction in nuclear matter of some 7F,[21] it would thus appear that our calculations of elastic and inelastic scattering are fairly insensitive to contributions from the nuclear interior.

The DW calculations of inelastic cross sections made with the complete form factor (27) and the potentials of Table II are compared to the data in Fig. 12. The values of the central-well deformation parameters β_ℓ deduced from adjusting the normalization of the calculations to match the data are indicated in the figure. These are in good agreement with those found[2] from complex-coupling calculations for the previous Minnesota data.[42] The largest discrepancy (30%) occurs for the 1.41 and 4.8 MeV states in ^{54}Fe, and is mostly due to the experimental discrepancies noted in Section II. As can be observed in Figs. 6 and 7, the curves for complex coupling agree closely with those for the complete form factor in the region of the maxima in the angular distributions. Since the calculations are normalized to the data in those regions, and since the present optical potentials were deduced from elastic data which agree fairly well with the data[47] used in Ref. 2, the present deformation parameters for the states in ^{58}Ni and ^{60}Ni should agree well with those found in Ref. 2; they agree within five percent.

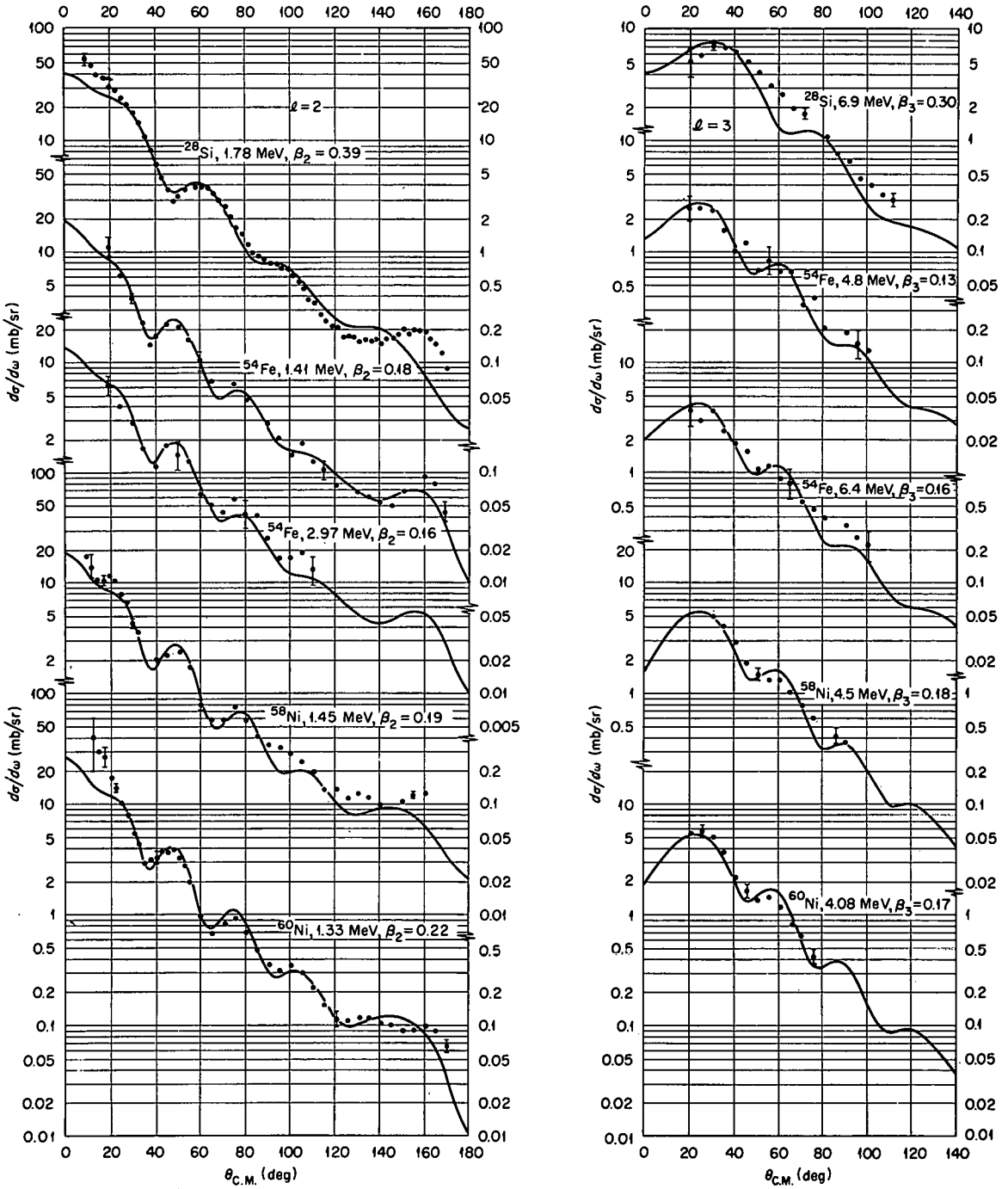

Figure 12. Inelastic cross-section data and DW predictions using complex-plus-spin-orbit coupling and the optical-model parameters of Table II. The deformation parameters indicated are those for the central potential.

As can be seen, the shape of the cross sections for the heavier nuclei is predicted rather well out to very large angles. The exceptions to this are the anomalous bump observed near 100° in the cross section for the 2^+ state in ^{58}Ni and the data at angles smaller than 20° for the 2^+ state in ^{60}Ni. The latter could be due to a systematic error in reducing the data, as discussed in Section II, but the former appears to be real. At 100°, any contaminant elastic peaks from ^{16}O and ^{12}C are separated by 2.5 MeV and 4.2 MeV, respectively, from the inelastic group corresponding to the 2^+ excitation in ^{58}Ni. The DW predictions for the states in ^{28}Si are poor, but little else can be said until a more successful fit is achieved to the elastic data for that target. The deformation parameters indicated for the ^{28}Si data are tentative at best. The prediction for the 6.9-MeV level observed in ^{28}Si is very bad and does not confidently identify the multipole order.

The inelastic asymmetry data and their DW predictions are shown in Fig. 13. The calculations are the same as those shown for the cross sections in Fig. 12. As was the case in the preliminary calculations for ^{28}Si and ^{60}Ni, the present form of the theory appears to give a good account of the large oscillations observed at large angles, but does not appear to reproduce the data at angles smaller than about 50° for iron and nickel and about 70° for silicon. The calculations using the complete form factor are invariably

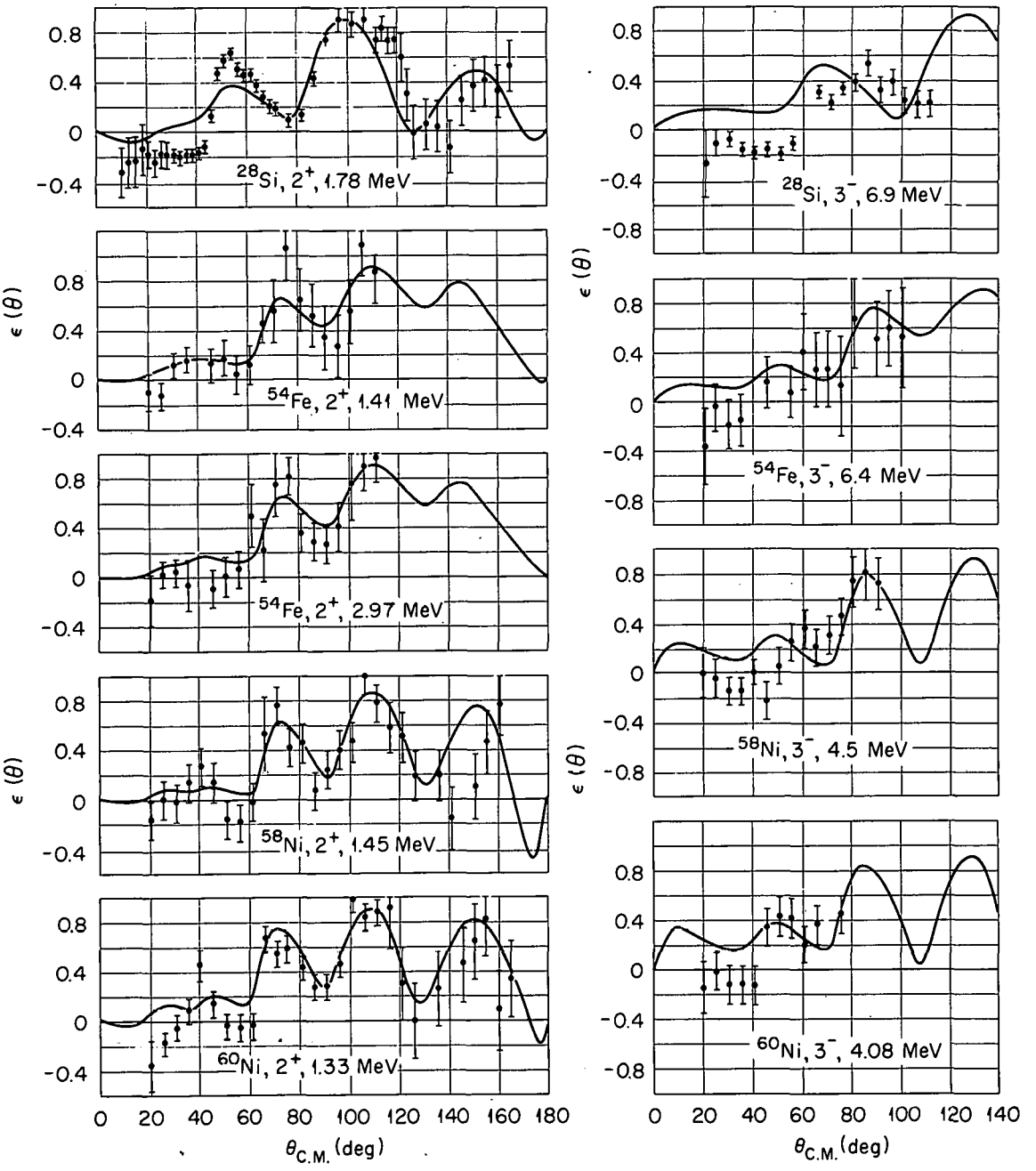

Figure 13. Inelastic asymmetry data and DW predictions using complex-plus-spin-orbit coupling and the optical-model parameters of Table II.

positive at small angles, say 20° to 30°, while the data for both 2^+ and 3^- excitations appear to be negative. The calculations for the two 2^+ states in ^{54}Fe do not seem to oscillate enough to reproduce the minima observed near 90°. This is reminiscent of the situation for the "good cross section" potential of Fig. 5 and leads one to suspect that the unmeasured, large-angle elastic polarization would not agree well with the optical-model curve in Fig. 11.

IV. DISCUSSION

We have undertaken to measure and analyze the asymmetry produced in the inelastic scattering of 40-MeV polarized protons and have had some qualified success in both endeavors. In the present Section we will comment briefly on the main results and suggest some ways in which this study might be improved.

Measurement of the elastic and inelastic scattering at large angles has proved an essential part of this work. Indeed, had the measurements covered only the forward hemisphere, we would have little evidence that our analysis of the inelastic asymmetry was on the right track. The elastic polarization data at large angles demand new values of the optical-model parameters which also produce a significant improvement in the predictions of inelastic asymmetry. At present it appears that more back-angle elastic polarization data will be necessary to establish the optimum parameter values for 40-MeV protons, or to decide whether or not the present form of the potential can in fact account simultaneously for the elastic cross section and polarization at all angles.

The intensity and polarization of our proton beam, and the overall energy resolution we achieved, were marginal for the collective excitations measured. To extend this study to non-collective transitions, considerably better resolution

would be necessary. Polarized proton sources for linear accelerators and cyclotrons, together with solid-state detectors or magnetic analysis of the scattered protons, afford exciting opportunities to explore excitations more amenable to a microscopic description. As was mentioned, there is evidence from lower-energy work[26] that the asymmetries for some low-lying 2^+ states in medium-weight nuclei show differences which do not appear to be explained within the framework of the collective model. Some of these excitations are fairly enhanced; each of the two 2^+ states in ^{54}Fe has a transition probability to the ground state B(E2) of approximately eight times the single-particle value. Thus, "microscopic effects" may show up in inelastic asymmetry measurements at medium energy for states which could be studied with only a modest improvement in the resolution and intensity achieved here.

Our measurements of inelastic asymmetry have distinguished between some collective-model interactions believed plausible for the present data. In particular, we find the collective-model generalization of the optical model to be successful for these data only when the effective interaction is derived from both real and imaginary parts of the optical potential. Because the inelastic asymmetry prediction is not insensitive to arbitrary variations in the imaginary form factor, the consistent improvement produced

by the collective-model prescription for the imaginary interaction is indeed striking. For higher-energy proton scattering, the impulse approximation yields a complex-valued effective interaction, and it has been expected that the interaction should also be complex-valued in a microscopic treatment for medium-energy protons.[14] The latter has not yet been investigated; the phenomenology of the real two-body force used in that treatment is just now being pioneered. However, the results here suggest that, for a microscopic description of the present inelastic asymmetry data, an imaginary contribution deserves some consideration even in the pioneering stage. Yet it is far from clear how such a contribution should be included. For example, it is not sufficient to multiply the complete two-body interaction by some factor $(1 + i\delta)$, where δ is a real parameter, since this would not change the asymmetry and affect only the normalization of the cross section.[14,6] To produce a difference in shape, the imaginary part of the effective interaction must have a different form than the real part.

The spin-dependent inelastic interaction we have investigated has proved remarkably successful for both the inelastic asymmetry and cross section at larger angles. But the worsened agreement with the asymmetry data it consistently produces at forward angles suggests that the interaction is not yet complete. This and the rough indication

that the strength of the present spin-orbit interaction is slightly greater than its "natural" strength, i.e. $\beta_\ell^{SO} \simeq 1.5\ \beta_\ell$, leads one to ask if the proper collective interaction should not also contain the more complicated terms which would arise from treating the form of the Thomas potential given in Eq. (28). However, it is difficult to estimate the effect of these terms short of carrying out full calculations with that interaction; such a study is now underway.[57] Alternatively, one could continue to examine the spin-orbit interaction phenomenologically. In particular the present form factor with the radial dependence $(1/r)\ (d^2/dr^2)\ f(x_S)$, where $f(x_S)$ is the Woods-Saxon shape factor, is relatively small at large r. It would be interesting to investigate the form $(d^2/dr^2)\ f(x_S)$, or perhaps simply a surface form $(d/dr)\ f(x_S)$. If the spin-orbit form factor is derived from the optical potential in the same way as one obtains the other collective-model form factors, the dependence $(d^2/dr^2)\ f(x_S)$ would correspond to a term in the optical potential for elastic scattering with the dependence $(d/dr)\ f(x_S)$. It would be desirable to try this combination in a consistent way, in which the parameters of $f(x_S)$ are determined by fitting the elastic data.

In short, then, the sensitivity of the inelastic asymmetry calculations is leading to refinements in the collective-model interaction investigated for the present data. The fact that these calculations require a very careful treatment of the

elastic distortion adds to the credibility of the distorted-waves treatment. Based on this experience, there is good reason to expect that future asymmetry or polarization measurements will provide valuable contributions to our understanding of the inelastic scattering of medium-energy protons.

V. ACKNOWLEDGEMENTS

I could not have done any of this single-handedly. I am grateful to my adviser at Minnesota for heading me off in a fruitful direction, and to my adviser at ORNL for ensuring the harvest. I owe my original interest in proton scattering to the former, N. M. Hintz, whose enthusiasm for the subject and perception of all its ramifications have been a potent source of inspiration. I am enormously indebted to the latter, A. Zucker, for his continuing interest and valuable advice in all of my endeavors, not only throughout this experiment but since the time I was an undergraduate participant at Oak Ridge, which dates back to 1956. My thesis work was done in the Electronuclear Division at the Oak Ridge National Laboratory, which is operated by the Union Carbide Corporation for the U. S. Atomic Energy Commission. This thesis arrangement was made possible by a graduate fellowship from the Oak Ridge Associated Universities, a courteous, generous, and opportunity-filled relationship which I encourage other northern graduate students to investigate promptly.

The experiment was performed by the ORIC polarization group, of which I was a member. The other members were E. E. Gross, B. J. Morton (from the University of Tennessee), and A. Zucker, all of whom contributed both advice and effort in major proportions. I am personally indebted to E. E. Gross

for countless consultations and for his continual encouragement during this project. The ORIC cyclotron operators performed gallantly in the desperate atmosphere produced by our experiment and constantly broke records for beam intensity. I am indebted to M. B. Marshall of the ORIC staff for his special interests and efforts in fabricating and installing the beam-optics system.

Most of the non-experimental things I've done at Oak Ridge (since undergraduate days) have been patiently explained to me by R. H. Bassel, who has lately moved to Brookhaven despite my wailing. In recent years, G. R. Satchler has contributed enormously to both my education and my projects. Most recently, R. M. Drisko has taken up the burden and, on one fine night in October of 1965, deformed the spin-orbit term for his code JULIE. His extensive guidance in subsequent applications to the data here has made the present analysis possible.

I am grateful to Jane Binkley for typing this manuscript and for an unknown number of improvements in English. The procedure for using the coupled-equations code was kindly explained to me by T. Tamura and C. Y. Wong. I have benefitted from a number of discussions of this work with R. M. Haybron and R. O. Ginaven.

VI. REFERENCES

1. B. Buck, Phys. Rev. 130, 712 (1963); F. G. Perey, R. J. Silva, and G. R. Satchler, Phys. Letters 4, 25 (1963); G. R. Satchler, R. H. Bassel, and R. M. Drisko, Phys. Letters 5, 256 (1963); J. K. Dickens, F. G. Perey, R. J. Silva, and T. Tamura, Phys. Letters 6, 53 (1963); M. Sakai, et al., Phys. Letters 8, 197 (1964); K. Yagi, et al., Phys. Letters 10, 186 (1964); J. Benveniste, A. C. Mitchell, B. Buck, and C. B. Fulmer, Phys. Rev. 133, B323 (1964); T. Tamura, in Nuclear Spectroscopy with Direct Reactions, I, Argonne National Laboratory Report 6848, p. 24, 1964 (unpublished); M. P. Fricke, ibid. p. 130; M. Sakai and T. Tamura, Phys. Letters 10, 323 (1964); G. C. Pramila, R. Middleton, T. Tamura, and G. R. Satchler, Nucl. Phys. 61, 448 (1965); S. F. Eccles, H. F. Lutz, and V. A. Madsen, Phys. Rev. 141, 1067 (1966); R. L. Robinson, J. L. C. Ford, Jr., P. H. Stelson, and G. R. Satchler, Phys. Rev. 146, 816 (1966); R. K. Cole, C. N. Waddell, R. R. Dittman, and H. S. Sandhu, Nucl. Phys. 75, 241 (1966); J. Stevens, H. F. Lutz, and S. F. Eccles, Nucl. Phys. 76, 129 (1966).

2. M. P. Fricke and G. R. Satchler, Phys. Rev. 139, B567 (1965).

3. A. Scott and M. P. Fricke, Phys. Letters 20, 654 (1966).

4. S. Hayakawa and S. Yoshida, Progr. Theoret. Phys. (Kyoto) 14, 1 (1955); D. M. Brink, Proc. Phys. Soc. (London) 68A , 994 (1955); J. S. Blair, Phys. Rev. 115, 928 (1959); E. Rost and N. Austern, Phys. Rev. 120, 1375 (1960).

5. R. H. Bassel, G. R. Satchler, R. M. Drisko, and E. Rost, Phys. Rev. 128, 2693 (1962).

6. G. R. Satchler, Nucl. Phys. 55, 1 (1964).

7. The inelastic scattering calculations given in this Thesis were made with a slightly amended version of the code JULIE, by R. M. Drisko (unpublished), with which it is possible to calculate a scattering amplitude for a deformed spin-orbit potential (Section III) and add it coherently to other amplitudes which are calculated conventionally. This version of the code differs from the code SALLY described in Ref. 5 by this feature and by the inclusion of the spin-orbit term in the distorting potential (as is discussed in Ref. 6). The elastic scattering calculations were made with the optical-model search code HUNTER of R. M. Drisko (unpublished).

8. F. G. Perey and G. R. Satchler, Phys. Letters 5, 212 (1963).

9. The progress of collective-model calculations for odd-mass nuclei has been reviewed by J. S. Blair, in Nuclear Spectroscopy with Direct Reactions, II, Argonne National Laboratory Report 6878, p. 143, 1964 (unpublished).

10. T. Tamura, Rev. Mod. Phys. 37, 679 (1965).

11. Microscopic descriptions of single-nucleon transitions were formulated by C. A. Levinson and M. K. Banerjee, Ann. of Physics 2, 471 (1957); 2, 499 (1957); 3, 67 (1958); and by N. K. Glendenning, Phys. Rev. 111, 1568 (1958). Collective transitions were treated in PWBA by L. S. Kisslinger, Phys. Rev. 129, 1316 (1963).

12. A. K. Kerman, H. McManus, and R. M. Thaler, Ann. of Physics 8, 551 (1959); R. M. Haybron and H. McManus, Phys. Rev. 136, B1730 (1964).

13. R. M. Haybron and H. McManus, Phys. Rev. 140, B638 (1965).

14. G. R. Satchler, Nucl. Phys. 77, 481 (1966).

15. N. K. Glendenning and M. Veneroni, Phys. Rev. 144, 839 (1966).

16. H. O. Funsten, N. R. Roberson, and E. Rost, Phys. Rev. 134, B117 (1964).

17. W. S. Gray, R. A. Kenefick, J. J. Kraushaar, and G. R. Satchler, Phys. Rev. 142, 735 (1966); M. B. Johnson, L. W. Owen, and G. R. Satchler, Phys. Rev. 142, 748 (1966).

18. M. P. Fricke, M.S. Thesis, University of Minnesota, 1964 (unpublished).

19. E. R. Flynn and R. H. Bassel, Phys. Rev. Letters 15, 168 (1965), and other references given there.

20. L. N. Blumberg, E. E. Gross, A. van der Woude, A. Zucker, and R. H. Bassel, Phys. Rev. 147, 812 (1966).

21. M. P. Fricke, E. E. Gross, B. J. Morton, and A. Zucker, Phys. Rev. (to be published).

22. Early measurements of the polarization and asymmetry in inelastic scattering have been reviewed by E. J. Squires, in Progress in Nuclear Physics, Vol. 8 (Macmillan, New York, 1960), p. 47.

23. P. Darriulat, J. M. Fowler, R. de Swiniarski, and J. Thirion, in Proceedings of the 2nd International Symposium on Polarization Phenomena of Nucleons, Karlsruhe, September 6-10, 1965, ed. P. Huber and H. Schopper (W. Rösch and Co., Bern, Germany, 1966), p. 342.

24. R. M. Craig, J. C. Dore, G. W. Greenlees, J. Lowe, and D. L. Watson, Nucl. Phys. 79, 177 (1966).

25. R. M. Craig, J. C. Dore, G. W. Greenlees, J. Lowe, and D. L. Watson, Nucl. Phys. (to be published).

26. A. Garin, C. Glashausser, A. Papineau, R. de Swiniarski, and J. Thirion, Phys. Letters 21, 73 (1966).

27. F. G. Perey, in Proceedings of the 2nd International Symposium on Polarization Phenomena of Nucleons, Karlsruhe, September 6-10, 1965, ed. P. Huber and H. Schopper (W. Rösch and Co., Bern, Germany, 1966), p. 191.

28. M. P. Fricke, E. E. Gross, B. J. Morton, and A. Zucker, in Proceedings of the International Conference on Nuclear Physics, Gatlinburg, Tennessee, September 12-17, 1966 (to be published); M. P. Fricke, R. M. Drisko, R. H. Bassel, E. E. Gross, B. J. Morton, and A. Zucker, Phys. Rev. Letters 16, 746 (1966); M. P. Fricke, E. E. Gross, B. J. Morton, and A. Zucker, Bull. Am. Phys. Soc. 11, 13 (1966).

29. L. N. Blumberg, E. E. Gross, A. van der Woude, and A. Zucker, Nucl. Instr. and Methods 39, 125 (1966).

30. R. S. Livingston and F. T. Howard, Nucl. Instr. and Methods 6, 1 (1960).

31. L. Rosen and J E. Brolley, Jr., Phys. Rev. 107, 1454 (1957).

32. B. J. Morton, R. H. Bassel, L. N. Blumberg, M. P. Fricke, E. E. Gross, A. van der Woude, and A. Zucker, Bull. Am. Phys. Soc. 11, 13 (1966); and to be published.

33. The design of the ORIC beam-handling system is described by E. D. Hudson, R. S. Lord, M. P. Fricke, and B. Duelli, in Oak Ridge National Laboratory Report TM-335, 1962 (unpublished).

34. Focusing conditions for bombarding the polarizer target, and the design of the Q6-Q7 quadrupole system, are due to E. E. Gross.

35. The calculations made for the analyzing magnet, and the symbols used here for its parameters, are consistent with those given by M. M. Bretcher, in Oak Ridge National Laboratory Report ORNL-2884, 1960 (unpublished). The theory of quadrupole lenses is indicated in Ref. 33.

36. A. A. Enge, Rev. Sci. Instr. 32, 662 (1961).

37. R. F. Sweet, Oak Ridge National Laboratory Report ORNL-3638, 1964 (unpublished).

38. T. J. Devlin, University of California Radiation Laboratory Report UCRL-9727, 1961 (unpublished). The code used in this work is a version which has been slightly modified from the above by E. E. Gross.

39. Private communication to E. E. Gross from J. C. Dore of the University of Birmingham; and R. M. Craig, J. C. Dore, G. W. Greenlees, J. S. Lilley, J. Lowe, and P. C. Rowe, Nucl. Instr. and Methods 30, 268 (1964).

40. L. Wolfenstein, Phys. Rev. 75, 1664 (1949).

41. E. Heiberg, U. Kruse, J. Marshall, L. Marshall, and F. Solmitz, Phys. Rev. 97, 250 (1955).

42. T. Stovall and N. M. Hintz, Phys. Rev. 135, B330 (1964).

43. The code SLAP (unpublished) was written by J. A. Biggerstaff and adapted to our needs by R. J. Leinius.

44. D. F. Measday, Nucl. Instr. and Methods 34, 353 (1965).

45. See, for example, R. T. Birge, Am. J. Phys. 7, 351 (1939).

46. The program to process the asymmetry data was coded by W. J. Roberts.

47. M. K. Brussel and J. H. Williams, Phys. Rev. 114, 525 (1959).

48. C. H. Poppe, R. Boyd, H. Liers, and J. H. Williams, Bull. Am. Phys. Soc. 10, 526 (1965).

49. F. G. Perey and A. M. Saruis, Nucl. Phys. 70, 225 (1965).

50. A. M. Lane, Phys. Rev. Letters 8, 171 (1962); Nucl. Phys. 35, 676 (1962).

51. F. G. Perey, Phys. Rev. 131, 745 (1963).

52. R. M. Haybron, Nucl. Phys. 79, 33 (1966).

53. N. Austern and J. S. Blair, Ann. of Physics (New York) 33, 15 (1965).

54. R. H. Bassel, private communication.

55. These calculations were made with the coupled-equations code of T. Tamura (unpublished).

56. G. R. Satchler, Nucl. Phys. (to be published).

57. R. M. Drisko, private communication.

VII. TABLES OF DATA

The elastic and inelastic cross section and asymmetry data for each target are given in the center-of-mass coordinate system. The inelastic data include results for the doublet near 4.8 MeV in ^{28}Si, which was not resolved in this work. The fractional error $\Delta\sigma/\sigma$ (where $\sigma = \sigma_{EX} \pm \Delta\sigma$) and the error $\Delta\epsilon$ (where $\epsilon = \epsilon_{EX} \pm \Delta\epsilon$) are the total relative probable errors defined in Section II-3. In addition to these, the "absolute" error in the normalization of the asymmetries is ± 1.8%, and the absolute error in the cross sections is ± 5.5% for iron and nickel and ± 6.8% for silicon.

$E_P^{LAB} = 40.0 \pm 0.4$ MeV

$^{28}Si + p$, Elastic

$\theta_{C.M.}$ (deg)	$\sigma_{C.M.}(\theta)$ (mb/sr)	$\Delta\sigma/\sigma$ (%)	$\epsilon(\theta)$	$\Delta\epsilon$
10.4	3465	± 2	.043	± .03
13.0	2636		.022	
15.6	2012		.000	
18.2	1545		-.042	
20.7	1044		-.088	± .01
23.3	657		-.110	
25.9	379		-.138	
28.5	216		-.196	
31.1	104		-.222	
33.7	57.5		-.105	
36.2	39.9	± 5	.241	
38.8	41.4	± 5	.462	
41.4	49.1	± 2	.529	
44.0	54.7		.471	
46.5	53.7		.413	
49.1	51.1		.366	
51.7	42.3		.292	
54.2	36.0		.242	
56.8	25.8		.215	
59.3	19.3		.201	
61.9	13.1		.185	± .05
64.4	9.73		.234	
67.0	7.04		.363	
69.5	5.96	± 3	.540	
72.0	5.25		.737	
74.6	4.73			
77.1	4.63		.949	
79.6	4.39			
82.1	4.08		.931	
84.6	3.61			
87.1	3.11		.863	
89.6	2.65			
92.2	2.23		.789	
94.6	1.68			
97.1	1.35		.651	
99.6	1.07			
102.1	.883		.576	
104.6	.713			

$^{28}Si + p$, Elastic (con't.)

$\theta_{C.M.}$ (deg)	$\sigma_{C.M.}(\theta)$ (mb/sr)	$\Delta\sigma/\sigma$ (%)	$\epsilon(\theta)$	$\Delta\epsilon$
107.1	.616	± 3	.404	± .05
109.6	.566	↓		
112.0	.528	± 5	.419	± .10
114.5	.508	|	.374	|
116.9	.471	|	.394	|
119.4	.445	|	.413	|
121.9	.399	|	.545	|
124.3	.359	|	.619	|
126.8	.307	|	.595	|
129.2	.260	|	.723	|
131.6	.212	|	.629	|
134.1	.170	|	.597	|
136.5	.150	|	.738	|
139.0	.119	|	.665	↓
141.4	.114	|	.423	± .15
143.8	.106	|	.336	|
146.2	.106	|	-.107	|
148.7	.115	↓	-.053	|
151.1	.125	± 10	-.189	|
153.5	.140	|	-.506	|
155.9	.127	|	-.460	|
158.3	.119	|	-.537	|
160.7	.125	|	-.497	↓
163.1	.103	|	-.340	± .20
165.6	.084	|	-.500	|
168.0	.068	|	-.741	↓
170.4	.042	↓		

$E_P^{LAB} = 40.0 \pm 0.4$ MeV

$^{28}Si + p$, Q = -1.78 MeV, 2^+

$\theta_{C.M.}$ (deg)	$\sigma_{C.M.}(\theta)$ (mb/sr)	$\Delta\sigma/\sigma$ (%)	$\epsilon(\theta)$	$\Delta\epsilon$
10.4	53.8	± 15	-.33	± .20
13.0	47.6	± 15	-.25	
15.6	39.8	± 10	-.24	
18.2	38.0	± 10	-.14	
20.8	30.7	± 5	-.18	± .10
23.3	28.7		-.25	
25.9	24.9		-.18	
28.5	21.1		-.19	
31.1	17.8	± 3	-.19	± .05
33.7	14.6		-.21	
36.3	11.1		-.19	
38.8	8.31		-.19	
41.4	6.31		-.17	
44.0	4.72		-.12	
46.6	3.64		.13	
49.1	2.91		.47	
51.7	3.23		.57	
54.2	3.66		.63	
56.8	3.68		.50	
59.4	3.90		.45	
61.9	3.86		.46	
64.5	3.79		.37	
67.0	3.41		.28	
69.5	2.97		.20	
72.1	2.59		.18	
74.6	2.09			
77.1	1.67		.09	
79.6	1.44			
82.2	1.16		.13	
84.7	.980			
87.2	.915		.43	
89.7	.875			
92.2	.802		.74	
94.7	.788			
97.2	.720		.91	± .10
99.7	.697			
102.2	.611		.87	
104.6	.534			

$^{28}Si + p$, Q = -1.78 MeV, 2^+ (con't.)

$\theta_{C.M.}$ (deg)	$\sigma_{C.M.}(\theta)$ (mb/sr)	$\Delta\sigma/\sigma$ (%)	$\epsilon(\theta)$	$\Delta\epsilon$
107.1	.461	± 3	.90	± .10
109.6	.379	↓		↓
112.1	.345	↓	.74	
114.5	.275	± 5	.83	
117.0	.235	↓	.73	
119.5	.212	↓	.74	↓
121.9	.208	↓	.60	± .20
124.4	.170	↓	.30	↓
126.8	.177	↓	-.01	↓
129.2	.168	↓	↓	↓
131.7	.158	↓	.06	↓
134.1	.161	↓	↓	↓
136.6	.156	↓	.04	↓
139.0	.159	↓	↓	↓
141.4	.148	↓	-.13	↓
143.8	.161	↓	↓	↓
146.3	.167	↓	.25	↓
148.7	.180	↓	↓	↓
151.1	.199	↓	.37	↓
153.5	.184	↓	↓	↓
155.9	.197	↓	.41	↓
158.3	.192	↓	↓	↓
160.8	.189	↓	.33	↓
163.2	.164	↓	↓	↓
165.6	.148	↓	.53	↓
168.0	.119	↓	↓	
170.4	.088	↓		

$E_P^{LAB} = 40.0 \pm 0.4$ MeV

$^{28}Si + p$, $Q \sim -4.8$ MeV (unresolved doublet)

$\theta_{C.M.}$ (deg)	$\sigma_{C.M.}(\theta)$ (mb/sr)	$\Delta\sigma/\sigma$ (%)	$\epsilon(\theta)$	$\Delta\epsilon$
20.8	1.80	± 40	-.07	± .50
26.0	2.20	± 25	-.09	± .20
31.2	2.21	± 15	-.14	± .10
36.3	2.02	± 10	-.09	
41.5	1.55		-.36	
46.6	1.27		-.35	
51.8	1.14		-.30	
56.9	.920		-.18	
62.0	.800			
67.1	.541		.00	
72.2	.405		.16	
77.2	.366		.58	
82.3	.295		.75	
87.3	.281		.50	
92.3	.208		.62	
97.3	.180	± 5	.61	
102.3	.132		.60	
107.2	.118		.32	
112.2	.112		-.11	± .15
117.1	.104		.27	
122.0	.108		-.25	
126.9	.092		.15	
131.8	.097		.29	
136.6	.097		.62	
141.5	.109		.29	
146.3	.118		.47	
151.1	.150		.09	
156.0	.159		.29	± .10
165.6	.130		.50	± .10

$E_P^{LAB} = 40.0 \pm 0.4$ MeV

$^{28}Si + p$, $Q \sim -6.9$ MeV, (3^-)

$\theta_{C.M.}$ (deg)	$\sigma_{C.M.}(\theta)$ (mb/sr)	$\Delta\sigma/\sigma$ (%)	$\epsilon(\theta)$	$\Delta\epsilon$
20.8	5.11	± 30	-.26	± .25
26.0	5.86	± 15	-.11	± .10
31.2	7.07	± 10	-.08	± .05
36.4	6.90	↓	-.16	↓
41.5	6.29	↓	-.19	↓
46.7	4.99	↓	-.16	↓
51.8	4.11	↓	-.20	↓
56.9	3.10	↓	-.11	↓
62.1	2.62	↓		↓
67.2	1.95	↓	.30	↓
72.2	1.70	↓	.22	↓
77.3	1.29	↓	.33	↓
82.3	1.07	↓	.39	↓
87.4	.758	↓	.53	± .10
92.4	.644	↓	.31	↓
97.4	.449	↓	.38	↓
102.3	.391	↓	.23	↓
107.3	.322	± 15	.20	↓
112.2	.290	± 15	.21	↓

$E_P^{LAB} = 40.0 \pm 0.4$ MeV

$^{54}Fe + p$, Elastic

$\theta_{C.M.}$ (deg)	$\sigma_{C.M.}$ (A) (mb/sr)	$\Delta\sigma/\sigma$ (%)	$\epsilon(\theta)$	$\Delta\epsilon$
10.2	8138	± 2		
12.7	4482			
15.3	2704		-.035	± .01
17.8	1581			
20.4	801.5		-.097	± .05
22.9	288.7			
25.5	78.4	± 5	-.347	
28.0	31.9	± 10		
30.6	51.8	± 5	.346	
33.1	102.0	± 2		
35.6	135.5		.271	± .01
38.2	137.7			
40.7	125.7		.109	
43.3	98.9			
45.8	69.5	± 3	-.010	
48.3	42.8			
50.9	24.8		-.097	± .02
53.4	15.2			
55.9	12.2		.435	
58.4	12.7			
61.0	14.4		.769	
63.5	15.3			
66.0	15.3		.610	
68.5	13.1			
71.1	10.4		.484	
73.6	8.03			
76.1	5.53		.324	
78.6	4.12			
81.1	3.17		.272	± .05
83.6	2.53	± 5		
86.1	2.49		.554	
88.6	2.68			
91.1	2.57		.939	
93.6	2.48			
96.1	2.31		.948	
98.6	2.03			
101.1	1.60		.973	
103.6	1.30			

^{54}Fe + p, Elastic (con't.)

$\theta_{C.M.}$ (deg)	$\sigma_{C.M.}(\theta)$ (mb/sr)	$\Delta\sigma/\sigma$ (%)	$\epsilon(\theta)$	$\Delta\epsilon$
106.1	1.05	± 5	.871	± .05
108.6	.748	↓		↓
111.1	.606	↓	.782	↓
113.5	.508	± 10		
116.0	.497	± 10		
118.5	.474	|		
121.0	.467	|		
123.4	.503	|		
125.9	.521	|		
128.4	.503	|		
130.9	.446	|		
133.3	.408	|		
135.8	.339	|		
138.3	.259	|		
140.7	.198	|		
143.2	.169	|		
145.6	.137	|		
148.1	.143	|		
150.6	.174	↓		
153.0	.204	± 15		
155.5	.238	|		
157.9	.267	|		
160.4	.280	|		
162.8	.301	|		
165.3	.309	|		
167.7	.271	|		
170.2	.250	↓		

$E_P^{LAB} = 40.0 \pm 0.4$ MeV

$^{54}Fe + p$, Q = -1.41 MeV, 2^+

$\theta_{C.M.}$ (deg)	$\sigma_{C.M.}(\theta)$ (mb/sr)	$\Delta\sigma/\sigma$ (%)	$\epsilon(\theta)$	$\Delta\epsilon$
20.4	10.76	± 20	-.10	± .15
25.5	5.94	± 10	-.13	± .10
30.6	3.68	± 10	.12	↓
35.7	2.26	± 20	.16	↓
40.7	1.69	↓	↓	↓
45.8	2.14	↓	.13	± .15
50.9	2.06	↓	.17	↓
55.9	1.55	↓	.04	↓
61.0	1.02	↓	.12	↓
66.0	.659	↓	.45	↓
71.1	↓	↓	.55	± .25
76.1	.634	↓	1.06	↓
81.1	.441	↓	.64	↓
86.1	↓	↓	.52	↓
91.1	.282	↓	.34	↓
96.1	.204	↓	.27	↓
101.1	.143	↓	.55	↓
106.1	.181	↓	1.09	↓
111.1	.124	↓	.87	↓
116.0	.105	↓	↓	↓
121.0	.075	↓	↓	↓
130.9	.067	↓	↓	↓
135.8	.060	↓	↓	↓
140.7	.053	↓	↓	↓
145.7	.050	± 40	↓	↓
150.6	.067	↓	↓	↓
160.4	.090	↓	↓	↓
165.3	.078	↓	↓	↓
170.2	.044	↓	↓	↓

$E_P^{LAB} = 40.0 \pm 0.4$ MeV

$^{54}Fe + p$, Q = -2.97 MeV, 2^+

$\theta_{C.M.}$ (deg)	$\sigma_{C.M.}(\theta)$ (mb/sr)	$\Delta\sigma/\sigma$ (%)	$\epsilon(\theta)$	$\Delta\epsilon$
20.4	6.09	± 20	-.18	± .20
25.5	3.94	↓	.03	± .10
30.6	2.71	↓	.05	± .10
35.7	1.67	± 30	-.03	± .20
40.7	1.12	↓		
45.8	1.74	↓	-.09	± .15
50.9	1.46	↓	.01	↓
56.0	1.27	↓	.07	↓
61.0	.647	↓	.50	± .25
66.1	.513	↓	.22	↓
71.1	.433	↓	.75	↓
76.1	.574	↓	.82	± .15
81.1	.421	↓	.36	↓
86.2	.406	↓	.29	↓
91.2	.259	↓	.27	↓
96.2	.169	↓	.41	± .20
101.1	.169	↓	.76	± .30
106.1	.184	↓	.90	± .20
111.1	.133	↓	.97	± .20

$E_P^{LAB} = 40.0 \pm 0.4$ MeV

$^{54}Fe + p$, Q = -4.8 MeV, 3^-

$\theta_{C.M.}$ (deg)	$\sigma_{C.M.}(\theta)$ (mb/sr)	$\Delta\sigma/\sigma$ (%)
20.4	2.35	± 30
25.5	2.40	↓
30.6	2.26	↓
35.7	1.52	↓
40.8	.98	↓
45.8	1.13	↓
50.9	.64	↓
56.0	.79	↓
61.0	.62	↓
66.1	.62	↓
71.1	.32	↓
76.2	.37	↓
81.2	.20	↓
91.2	.18	↓
96.2	.14	↓
101.2	.12	↓

$E_P^{LAB} = 40.0 \pm 0.4$ MeV

$^{54}Fe + p$, Q = -6.4 MeV, 3^-

$\theta_{C.M.}$ (deg)	$\sigma_{C.M.}(\theta)$ (mb/sr)	$\Delta\sigma/\sigma$ (%)	$\epsilon(\theta)$	$\Delta\epsilon$
20.4	3.62	± 30	-.36	± .30
25.5	2.89		-.04	± .20
30.6	3.53		-.18	
35.7	2.30		-.15	
40.8	1.77			
45.9	1.52		.15	
50.9	1.05			
56.0	1.12		.07	
61.1	.86		.40	± .30
66.1	.77		.26	
71.1	.53		.26	
76.2	.45		.13	± .40
81.2	.38		.67	± .40
91.2	.32		.51	± .30
96.2	.25		.59	± .30
101.2	.21		.52	± .40

$E_P^{LAB} = 40.0 \pm 0.4$ MeV

$^{58}Ni + p$, Elastic

$\theta_{C.M.}$ (deg)	$\sigma_{C.M.}(\theta)$ (mb/sr)	$\Delta\sigma/\sigma$ (%)	$\epsilon(\theta)$	$\Delta\epsilon$
10.2	7727	± 2	.053	± .01
12.7	4395			
15.3	2525		-.106	
17.8	1429			
20.4	680		-.154	± .05
22.9	219			
25.4	53.5	± 10	-.544	
28.0	26.6	± 10		
30.5	54.0	± 2	.509	
33.1	107			
35.6	130		.217	± .01
38.1	133			
40.7	122		.067	
43.2	96.4	± 3		
45.7	68.8		-.173	
48.3	37.9			
50.8	23.7		-.102	
53.3	14.0			
55.9	12.3		.487	± .02
58.4	13.0			
60.9	14.6		.742	
63.4	15.4			
65.9	15.9		.504	
68.5	13.1			
71.0	11.2		.357	
73.5	8.26			
76.0	6.30		.146	
78.5	4.06			
81.0	3.30	± 5	.359	± .04
83.5	2.61			
86.0	2.37		.706	
88.5	2.32			
91.0	2.56		.986	
93.5	2.46			
96.0	2.38		.861	
98.5	1.99			
101.0	1.66		.838	± .08
103.5	1.32			

^{58}Ni + p, Elastic (con't.)

$\theta_{C.M.}$ (deg)	$\sigma_{C.M.}(\theta)$ (mb/sr)	$\Delta\sigma/\sigma$ (%)	$\epsilon(\theta)$	$\Delta\epsilon$
106.0	1.02	± 5	.673	± .08
108.5	.690	↓		↓
111.0	.615	± 10	.334	
113.5	.440			
115.9	.473		.505	
118.4	.460			
120.9	.511		.554	
123.4	.54			
125.9	.54		.658	± .10
128.3	.46			
130.8	.44		.855	
133.3	.31			
135.7	.32		.758	
138.2	.25			
140.7	.20		.839	± .15
143.1	.13			
145.6	.084			
148.1	.11			
150.5	.14		.410	
153.0	.13			
155.4	.22		.254	
157.9	.21			
160.4	.26		-.113	
167.7	.23			
170.2	.20	↓		

$E_P^{LAB} = 40.0 \pm 0.4$ MeV

$^{58}Ni + p$, Q = -1.45 MeV, 2^+

$\theta_{C.M.}$ (deg)	$\sigma_{C.M.}(\theta)$ (mb/sr)	$\Delta\sigma/\sigma$ (%)	$\epsilon(\theta)$	$\Delta\epsilon$
10.2	17.5	± 40		
12.7	14.0	± 30		
15.3	10.8	± 20	.31	± .40
17.8	10.4	± 10		
20.4	11.5		-.16	± .15
22.9	10.5			
25.4	7.95		.00	
28.0	6.72			
30.5	4.33		-.02	
33.1	3.58			
35.6	2.34		.14	
40.7	2.06		.27	
45.7	2.23		.14	
50.8	2.39		-.16	
55.9	1.77		-.18	
60.9	.804		-.02	
65.9	.586		.53	± .30
71.0	.576		.76	± .15
76.0	.750		.42	
81.0	.568		.46	
86.0	.412	± 5	.07	
91.0	.345		.24	
96.0	.323		.39	
101.0	.286		.47	
106.0	.242		1.02	
111.0	.195		.78	
115.9	.133		.58	± .20
120.9	.135	± 10	.51	
125.9	.112		.19	
130.8	.126			
135.7	.115		.19	
140.7	.099		-.16	± .25
150.5	.107		.11	
155.4	.119		.46	
160.4	.124		.78	

$E_P^{LAB} = 40.0 \pm 0.4$ MeV

$^{58}Ni + p$, Q = -4.5 MeV, 3^-

$\theta_{C.M.}$ (deg)	$\sigma_{C.M.}(\theta)$ (mb/sr)	$\Delta\sigma/\sigma$ (%)	$\epsilon(\theta)$	$\Delta\epsilon$
20.4	4.73	± 25	.00	± .20
25.4	5.15	± 15	-.05	± .15
30.5	4.90	↓	-.15	± .10
35.6	4.03	↓	-.15	↓
40.7	2.88	↓	.01	↓
45.7	1.83	↓	-.22	± .15
50.8	1.45	↓	.05	↓
55.9	1.30	↓	.25	↓
60.9	1.28	↓	.35	↓
65.9	.994	↓	.21	↓
71.0	.757	↓	.30	↓
76.0	.594	↓	.46	↓
81.0	.465	↓	.74	± .20
86.0	.409	↓	.80	↓
91.0	.357	↓	.72	↓

$E_P^{LAB} = 40.0 \pm 0.4$ MeV

^{60}Ni + p, Elastic

$\theta_{C.M.}$ (deg)	$\sigma_{C.M.}(\theta)$ (mb/sr)	$\Delta\sigma/\sigma$ (%)	$\epsilon(\theta)$	$\Delta\epsilon$
10.2	8371	± 2	.071	± .02
12.7	4542			
15.3	2770		-.062	
17.8	1506			
20.4	620		-.156	± .05
22.9	182			
25.4	42.9	± 10	-.564	
28.0	28.5	± 10		
30.5	75.8	± 2	.383	
33.1	134			
35.6	152		.153	± 0.03
38.1	148			
40.7	122		.015	
43.2	88.9			
45.7	53.8		-.186	
48.3	32.0			
50.8	16.6		-.068	
53.3	12.6			
55.8	12.4		.741	
58.4	15.5			
60.9	16.6		.684	
63.4	17.2			
65.9	15.2		.428	
71.0	9.11	± 3	.292	
73.5	6.36			
76.0	4.41		.237	
78.5	3.26			
81.0	2.64		.438	
83.5	2.85			
86.0	2.55		.950	
88.5	2.71			
91.0	2.49		1.00	± .05
93.5	2.27			
96.0	1.99		.955	
98.5	1.61			
101.1	1.31		.828	
103.5	.97	± 4		
106.0	.74		.433	

^{60}Ni + p, Elastic (con't.)

$\theta_{C.M.}$ (deg)	$\sigma_{C.M.}(\theta)$ (mb/sr)	$\Delta\sigma/\sigma$ (%)	$\epsilon(\theta)$	$\Delta\epsilon$
108.5	.55	± 4		
111.0	.49		.355	± .05
115.9	.40		.498	
118.4	.45			
120.9	.43		.669	
123.4	.46			
125.8	.40		.888	± .10
128.3	.37	± 5		
130.8	.29			
133.3	.29			
135.7	.21		.865	
138.2	.14			
140.7	.13			
143.1	.10			
145.6	.09		.547	
148.1	.09	± 10		
150.5	.11		.233	
153.0	.14			
155.4	.15		.048	
157.9	.22			
160.4	.22		-.391	
162.8	.22			
165.3	.21		-.483	
167.7	.17			
170.2	.14			

$E_p^{LAB} = 40.0 \pm 0.4$ MeV

$^{60}Ni + p$, Q = -1.33 MeV, 2^+

$\theta_{C.M.}$ (deg)	$\sigma_{C.M.}(\theta)$ (mb/sr)	$\Delta\sigma/\sigma$ (%)	$\epsilon(\theta)$	$\Delta\epsilon$
12.7	37.8	± 50		
15.3	28.3	± 30		
17.8	26.9	± 20		
20.4	16.7	± 15	-.35	± .20
22.9	14.1	± 10		
25.4	10.2		-.17	± .10
28.0	7.98			
30.5	5.51		-.05	
33.1	4.37			
35.6	2.94		.09	
38.1	3.19			
40.7	3.30		.46	
43.2	3.83			
45.7	3.70		.14	
48.3	3.85			
50.8	3.28		-.04	
53.3	2.75			
55.8	1.99		-.05	
58.4	1.69			
60.9	.970	± 5	-.04	
65.9	.679		.66	
71.0	.836		.54	
76.0	.951		.57	
81.0	.694		.43	
86.0	.483		.28	
91.0	.354		.28	
96.0	.314		.45	
101.0	.350		.97	
106.0	.306		.84	
111.0	.219		.88	
115.9	.151	± 15	.91	± .30
120.9	.116		.30	
125.8	.112		.00	
130.8	.120			
135.7	.117		.26	
140.7	.103			
145.6	.102		.46	
150.5	.090		.65	
155.4	.091		.82	
160.4	.100		.09	
165.3	.089		.34	
170.2	.066			

$E_P^{LAB} = 40.0 \pm 0.4$ MeV

$^{60}Ni + p$, Q = -4.08 MeV, 3^-

$\theta_{C.M.}$ (deg)	$\sigma_{C.M.}(\theta)$ (mb/sr)	$\Delta\sigma/\sigma$ (%)	$\epsilon(\theta)$	$\Delta\epsilon$
20.4	5.41	± 25	-.13	± .20
25.5	5.61	± 15	-.02	± .15
30.5	4.91	↓	-.11	↓
35.6	3.70	↓	-.11	↓
40.7	2.13	↓	-.12	↓
45.8	1.59	↓	.35	↓
50.8	1.33	↓	.44	↓
55.9	1.40	↓	.43	↓
60.9	1.17	↓	.21	↓
66.0	.821	↓	.37	↓
76.0	.408	↓	.45	↓

INTERNAL DISTRIBUTION

1. R. M. Drisko
2-21. M. P. Fricke
22. R. O. Ginaven
23. E. E. Gross
24. R. M. Haybron
25. E. V. Hungerford, III
26. R. S. Livingston
27. J. J. Malanify
28. B. J. Morton
29. F. G. Perey
30-31. L. A. Rayburn (ORAU)
32. G. R. Satchler
33. A. H. Snell
34. Taro Tamura
35. A. M. Weinberg
36. C. Y. Wong
37-41. A. Zucker
42-43. Central Research Library
44-45. Document Reference Section
46-55. Laboratory Records
56. Laboratory Records (ORNL-RC)
57. ORNL Patent Office
58-72. DTIE, AEC
73. Research and Development, ORO

EXTERNAL DISTRIBUTION

74. R. H. Bassel
Brookhaven National Laboratory

75. L. N. Blumberg
Brookhaven National Laboratory

76. E. J. Burge
Kings College

77. H. E. Conzett
Lawrence Radiation Laboratory, Berkeley

78. N. K. Glendenning
Lawrence Radiation Laboratory, Berkeley

79. G. W. Greenlees
University of Minnesota

80-104. N. M. Hintz
University of Minnesota

105. P. E. Hodgson
University of Oxford

106. E. Rost
University of Colorado

107. A. Scott
University of Georgia

108. J. Thirion
Saclay

109. A. van der Woude
University of Groningen